Materials Advances

ROYAL SOCIETY OF CHEMISTRY

PAPER

View Article Online
View Journal | View Issue



Cite this: *Mater. Adv.*, 2026, 7, 2068

# Large improvement in the charge storage performance of a $CoSb_2O_6$–reduced graphene oxide (rGO) composite – probing the role of rGO through experiments and theoretical analyses

Parul,[a] Surjit Sahoo,[b] M. Amrutha,[f] Satyajit Ratha,[c] Brahmananda Chakraborty*[de] and Saroj Kumar Nayak*[a]

Received 25th August 2025,
Accepted 6th January 2026

DOI: 10.1039/d5ma00956a

rsc.li/materials-advances

We present a detailed electrochemical comparison between cobalt antimony oxide ($CoSb_2O_6$) and its reduced graphene oxide (rGO) composite, prepared through a combination of hydrothermal and ultrasonic synthesis. The structural, morphological, and compositional properties of the as-synthesized material have been investigated through comprehensive characterization techniques. In a three-electrode configuration, the $CoSb_2O_6$/rGO composite exhibited a specific capacitance value of 1000 F $g^{-1}$ at a mass-normalized current of 2 A $g^{-1}$, which is at least 5-fold higher than that of pristine $CoSb_2O_6$ (*i.e.*, 195.5 F $g^{-1}$ at a mass-normalised current of 2 A $g^{-1}$). It shows a high capacity retention of 93.18% over 3000 cycles. We have also tested a two-electrode symmetric device, fabricated from the $CoSb_2O_6$/rGO composite, which shows a specific capacitance of 227.79 F $g^{-1}$ at a mass-normalised current of 1 A $g^{-1}$. The $CoSb_2O_6$/rGO composite yields energy and power densities of 38.28 Wh $kg^{-1}$ and 10.08 kW $kg^{-1}$, respectively, and exhibits a cyclic stability of 98.54% even after 10 000 cycles. Furthermore, we have employed density functional theory simulations to elucidate the structure and electronic characteristics of pristine $CoSb_2O_6$ and $CoSb_2O_6$/rGO composite systems. The enhancement in the electronic states near the Fermi level, resulting from the charge transfer from rGO to $CoSb_2O_6$, indicates improved conductivity of the $CoSb_2O_6$/rGO composite system. The considerably lower diffusion energy barrier and enhanced quantum capacitance of $CoSb_2O_6$/rGO compared to $CoSb_2O_6$ contribute to the superior supercapacitance performance, which supports our experimental findings.



## 1. Introduction

The demand for efficient, high-performance energy storage devices has become more important for powering a wide range of applications, including portable devices, electric cars, and smart city infrastructure. Supercapacitors have drawn significant interest because of their high power density, extended life cycle, and rapid charging time.[1] Nevertheless, conventional supercapacitors frequently experience bottlenecks in terms of energy density, prompting the addition of innovative materials to improve their performance.[2] Recently, there has been growing interest in utilizing hybrid materials to enhance charge storage performance. Despite the potential of these hybrid materials, issues persist in optimizing the energy–power spectrum for the device.[3] Different types of electrode materials have been investigated for supercapacitors, *e.g.*, carbonaceous materials, transition metal oxides (TMOs), and transition metal chalcogenides (TMCs). TMOs such as $V_2O_5$,[4] NiO,[5] $MoO_2$,[6] and $MnO_2$[7] exhibit rich redox mechanisms, making them suitable for the fabrication of a pseudocapacitive electrode.[8] Many binary metal oxides or some battery-type materials like $NiCo_2O_4$,[9] $CuFeS_2$,[10] $CuFe_2O_4$,[11] $CuCo_2O_4$,[12] and $CuWO_4$[13] have been reported to show good electrochemical performance for supercapacitors. With the rapid development of wearable, portable, and flexible electronic devices, there is a need for high-performance supercapacitors that combine long cycle stability, high power density, operational safety, and mechanical flexibility for practical applications. Recent works have shown that multifunctional electrodes, such as $Cu_3Mo_2O_9$

[a] *Indian Institute of Technology Bhubaneswar, Argul, Jatani, Khordha, Odisha-752050, India. E-mail: nayaks@iitbbs.ac.in*
[b] *Centre for Interdisciplinary Research, SRM University-AP, Amaravati, Andhra Pradesh 522240, India*
[c] *Institute of Technical Education and Research, S'O'A Deemed to be University, Bhubaneswar, Odisha, 751030, India*
[d] *High Pressure & Synchrotron Radiation Physics Division, Bhabha Atomic Research Centre, Trombay, Mumbai-400085, India. E-mail: brahma@barc.gov.in*
[e] *Homi J Bhabha National Institute, Bhabha Atomic Research Centre, Trombay, Mumbai-400085, India*
[f] *Department of Physics, Karpagam Academy of Higher Education (Deemed to be University), Coimbatore-641021, India*

nanostructures, are used in self-powered integration systems.[14] So, to improve the electrochemical performance, we need to focus on key factors like high surface area, pore size distribution, and cyclic stability of the electrode materials. EDLCs (electric double-layer capacitors showing surface adsorption at the electrode and electrolyte interface) typically exhibit high specific power and long cycle life, while pseudocapacitors (which rely on reversible fast redox reactions) have an improved specific energy profile. Combining these two materials will integrate the electrochemical functionalities in a single system and contribute to the development of more sustainable energy storage solutions for the future, thus achieving a very good power–energy (storage property) balance along with good cycle performance (lifetime of the material/device).[15] Moreover, hydrogel-based electrolytes such as PVA and S-PANa hydrogels have enabled flexible and safe devices that further expand practical applications.[16] Such reports highlight the growing importance of a versatile system for integration and next-generation energy storage technologies.

Within this expanding materials landscape, metal antimonates have emerged as a new class of promising electrode materials due to their stable crystal structure and strong faradaic redox activity. Here, we have synthesized cobalt antimony oxide, a pseudocapacitive material, and prepared its composite with reduced graphene oxide, aiming to improve the charge storage performance of the supercapacitor. We systematically optimize the weight percentage of reduced graphene oxide (*i.e.*, variation within 5% to 20% by weight of cobalt antimony oxide) and observe the change in electrochemical performance depending on the variation of the rGO content.[17] According to the reported literature, $CoO_x$,[18] $Co_3O_4$,[19,20] Sb-doped $Co_3O_4$,[21] and $Sb_2O_3$[22] show potential applications in various fields like energy storage, catalysis, and gas sensing.[23] $Co_3O_4$, with multiple morphologies, has been widely used in supercapacitor applications. Using the successive ionic layer adsorption and reaction (SILAR) method, a thin cobalt oxide film on a copper substrate exhibited a specific capacitance of 165 F $g^{-1}$.[18] In another work, porous $Co_3O_4$ nanocubes were synthesized by a hydrothermal method, yielding a specific capacitance of 430.6 F $g^{-1}$.[19] Furthermore, electrodeposited cobalt oxide on a copper substrate exhibited a specific capacitance of 235 F $g^{-1}$.[20] $Co^{2+}$ induced deposition in an $Sb_2O_5$/rGO composite showed enhanced interfacial interactions, showing potential for high-performance Li-ion/Na-ion storage applications.[24] The incorporation of antimony enhances the electrochemical performance of the electrode. Sb can form binary and ternary alloys with metals like cobalt, as in $CoSb_2O_6$, which enhances both structural integrity and conductivity, leading to improved electrochemical performance. It has been observed that Sb can act as an essential dopant species, which can tune the electrochemical properties of the electrode material.[21] Cobalt antimony oxide ($CoSb_2O_6$), which has a rutile-type structure,[23] presents intriguing applications in both sodium- and lithium-ion batteries as an anode active material,[25] catalysis, and the detection of various types of gases in sensors.[26] However, the inclusion of antimony enhances the surface area, generates an increased number of redox-active sites, and improves the stability of the electrode, significantly strengthening the electrochemical performance. One of the strategic steps to further enhance the cycle life of $CoSb_2O_6$ (a pseudocapacitive material) is by combining it with a carbonaceous material like reduced graphene oxide (because of its high electrical conductivity, large surface area, and chemical stability)[27] to form a composite/hybrid system. Several reports have observed that pristine metal oxides perform poorly compared with their rGO composites, indicating the significance of rGO in a composite/hybrid system. Despite these promising features, reports on the systematic optimization of $CoSb_2O_6$–rGO composite electrodes for supercapacitor applications are rare. Combining cobalt antimony oxide nanoparticles with a reduced graphene oxide substrate creates a three-dimensional conductive structure with improved mechanical and electrochemical stability, which has not been thoroughly explored. Addressing these gaps is critical for identifying the optimal composite structure and maximizing the redox activity of $CoSb_2O_6$ while benefiting from the excellent conductivity of rGO. Furthermore, the synergistic effect of rGO and cobalt antimony oxide, in the as-obtained composite, resulted in high electrochemical performance.

In this work, we compare the electrochemical performances of pristine cobalt antimony oxide and its rGO composite using state-of-the-art analytical methods. First, we discuss the detailed synthesis method for preparing the composite, which combines a hydrothermal reaction and ultrasonic treatment. In the next step, we perform detailed structural and morphological analyses on the samples to assess their dimensionality, crystal structure, and purity. Afterwards, we carry out detailed electrochemical analyses to determine the charge storage properties of the material in both three- and two-electrode configurations in an aqueous electrolyte medium.[28] To validate our experimental findings and gain insight into the electronic properties and the interaction between $CoSb_2O_6$ and rGO, we implemented first-principles calculations based on density functional theory (DFT).

## 2. Experimental section

### 2.1 Chemicals

Cobalt(ous) chloride hexahydrate [$CoCl_2{\cdot}6H_2O$, 99%] and antimony trichloride [$SbCl_3$, 99%] were procured from the Central Drug House Pvt Ltd (India). Ammonia solution [$NH_3$, 25%] and *N*-methyl-2-pyrrolidone [$C_5H_9NO$, 99.7%] were procured from Molychem, India. Graphene oxide [15–20 sheets] was purchased from Sigma-Aldrich. Poly(vinylidene fluoride) (PVDF) powder [$(-CH_2CF_2-)]_n$ and conductive carbon black [99+%, C] were procured from Alfa Aesar, India. All chemicals were of analytical grade and used without any further purification/modification.

### 2.2 Synthesis of cobalt antimony oxide ($CoSb_2O_6$)

A hydrothermal approach was used to synthesize cobalt antimony oxide.[29] First, solutions of 0.1 M cobalt chloride (dissolved in 20 ml of distilled water) and 0.1 M antimony trichloride (dissolved in 40 ml of distilled water) were combined and mixed in a beaker containing a total amount of 100 ml of distilled water, followed by ultrasonication for 10 minutes. Subsequently, the

beaker was placed on a magnetic stirrer, and ammonia solution was gradually added until the pH reached approximately 9. The obtained solution was transferred to a Teflon-lined stainless-steel autoclave and placed in a digital hot-air oven for 16 hours at a temperature of 160 °C. Then, the product was centrifuged with ethanol and water repeatedly until the pH became neutral. Once all these procedures were completed, the sample was dried in an oven for 8 hours at a temperature of 80 °C. Lastly, the product was calcined in a furnace for 5 hours at 500 °C to remove volatile substances and obtain a stable product.

### 2.3 Synthesis of the cobalt antimony oxide/reduced graphene oxide ($CoSb_2O_6$/rGO) composite

The cobalt antimony oxide/reduced graphene oxide composite was prepared using the ultra-sonication-assisted physical mixture method.[30] Here, we synthesized different cobalt antimony oxide/reduced graphene oxide composites by varying the weight percentage of rGO ($CoSb_2O_6$–5% rGO, $CoSb_2O_6$–10% rGO, $CoSb_2O_6$–15% rGO, $CoSb_2O_6$–20% rGO). Firstly, different weight percentages (*i.e.*, 5%, 10%, 15%, and 20%) of graphene oxide powder and the prepared cobalt antimony oxide nanoparticles were dispersed in ethanol by ultrasonication for 30 minutes (at 10-min intervals), which promoted exfoliation of rGO sheets and facilitated uniform anchoring of the $CoSb_2O_6$ particles onto the surface of rGO. Then the mixture was ground for 2 hours at room temperature to ensure uniform dispersion of $CoSb_2O_6$ particles on rGO sheets, and the reduction of graphene oxide was achieved by calcining the composite mixture for 1 h at 200 °C. Thus, the cobalt antimony oxide/reduced graphene oxide composite was obtained as the final product. The schematic diagram of the synthesis of cobalt antimony oxide and its rGO composite is shown in Fig. 1.

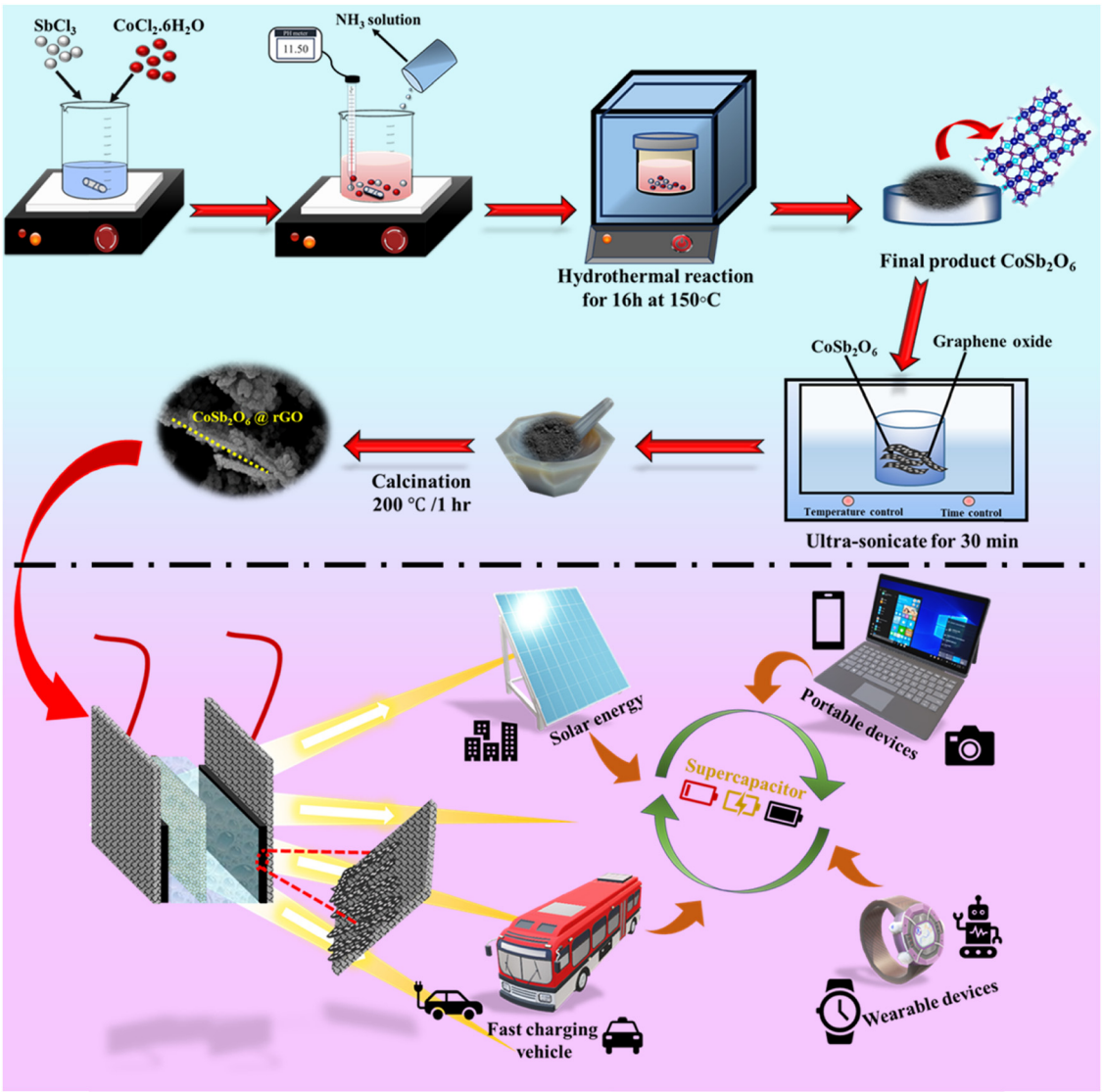


Fig. 1 Schematic representation of the preparation process of nanostructured $CoSb_2O_6$ and $CoSb_2O_6$-reduced graphene oxide composite materials, along with their future applications.

### 2.4 Physical characterization

The XRD analyses were conducted using a Bruker D8 Advance X-ray diffractometer (operating at 40 kV and 40 mA, with Ni-filtered Cu-$K_\alpha$ radiation). Surface morphology was studied by field emission scanning electron microscopy (Merlin Compact with Gemini 1 electron column). An Oxford Instruments EDX spectrometer was used for energy dispersive X-ray spectroscopy (EDX). The chemical composition of pristine $CoSb_2O_6$ and the $CoSb_2O_6$–15% rGO composite was analyzed by X-ray photoelectron spectroscopy (XPS) using a Thermo Fisher Scientific ESCALAB instrument. The surface area and pore volume of cobalt antimony oxide and its reduced graphene oxide composites ($CoSb_2O_6$–5% rGO, $CoSb_2O_6$–10% rGO, $CoSb_2O_6$–15% rGO, and $CoSb_2O_6$–20% rGO) were determined using Brunauer–Emmett–Teller (BET) analysis explicitly using a Quantachrome Nova 2200 instrument. Additionally, high-resolution morphological, elemental, and compositional information was obtained using high-resolution transmission electron microscopy (HR-TEM, JEOL JEM 2100 Plus). Room temperature Raman spectra were recorded using a Renishaw InVia Raman microscope with 532 nm laser excitation.

### 2.5 Electrochemical characterization

All electrochemical characterizations (cyclic voltammetry, galvanostatic charge–discharge cycling, and electrochemical impedance spectroscopy) were conducted using a multi-channel BioLogic electrochemical workstation (VSP-300). Here, nickel foam was used as the substrate for all as-synthesized materials. Initially, nickel foam was cleaned with diluted hydrochloric acid in a volume ratio of 1 : 3 and then gently washed with deionized water. After that, it was dried for 6 hours at 80 °C. For the electrode coating, a slurry was prepared in a weight ratio of 80 : 15 : 5. This included an 80% weight ratio of the active material, a 15% weight ratio of carbon black as the conductive material, in order to reduce the effect of the binder, and a 5% weight ratio of PVDF as the binding material, and the mixture was homogenously dispersed by using *N*-methyl-2-pyrrolidone (NMP). The slurry was mixed until a homogeneous mixture was obtained. Then, a slurry coating method (using the brush-paint technique) was employed to coat the nickel foam, followed by drying overnight at 80 °C. The mass loading for cobalt antimony oxide and its reduced graphene oxide composites was ~1 mg. These steps were consistently applied to all rGO composites.

Three-electrode measurements were performed on cobalt antimony oxide and its reduced graphene oxide composites. The working electrode was coated on the nickel foam, with Ag/AgCl as the reference electrode and a platinum mesh electrode as the counter electrode. 1 M aqueous sodium sulphate was used as the electrolyte for all electrochemical measurements. A two-electrode (symmetric) configuration was employed to evaluate the charge storage performance of the $CoSb_2O_6$–15% rGO composite, where a glass fiber membrane/pre-filter (purchased from Merck Millipore Ltd) was used as the separator to isolate the electrodes. The specific capacitance ($C_{sp}$) values of cobalt antimony oxide and its reduced graphene oxide composite electrodes were calculated from the cyclic voltammetry profiles and galvanostatic charge–discharge cycles using eqn (1) and (2), respectively:[31]

$$C_{sp} = \left(\int (I\,dV)/2(s \times m \times \Delta V)\right) \quad (1)$$

$$C_{sp} = (I \times \Delta t)/(\Delta V \times m) \quad (2)$$

The specific energy density ($E_d$) and specific power density ($P_d$) of the $CoSb_2O_6$–15% rGO symmetric device were calculated using eqn (3) and (4), respectively:[32]

$$E_d = (1/2 \times C_{sp} \times (\Delta V)^2)/3.6 \quad (3)$$

$$P_d = E_d/\Delta t \times 3600 \quad (4)$$

where $C_{sp}$ is the specific capacitance (F $g^{-1}$), $I$ is the current (mA), $s$ is the scan rate (mV $s^{-1}$), and $m$ is the mass loaded onto the working electrodes (g). $\Delta V$ is the active potential window (V). $\Delta t$ is the discharge time (s), $E_d$ is the specific energy density (Wh $kg^{-1}$), and $P_d$ is the particular power density (W $kg^{-1}$).

### 2.6 Computational details

All simulations were conducted using density functional theory (DFT) within the context of the projector-augmented wave (PAW) method[33] employing the Vienna *ab initio* simulation package (VASP).[34] The generalized gradient approximation (GGA) method[35] was employed to describe the exchange–correlation function, which accounts for ion–electron interactions. The structures were optimized until the force and energy convergence thresholds reached 0.01 eV $Å^{-1}$ and $10^{-5}$ eV, respectively. The cut-off energy for the plane wave basis set expansion was set to 500 eV. A gamma-centred *k*-point mesh with grids of 4 × 5 × 1 was used for sampling the reciprocal space. To eliminate periodic interactions, a vacuum spacing of 30 Å was introduced above the surface of the monolayer in the supercell. Moreover, Grimme's DFT-D2 dispersion correction method[36] was applied to account for van der Waals (vdW) interactions effectively.

## 3. Results and discussion

### 3.1 Structural, morphological, and elemental analyses

Hereafter, $CoSb_2O_6$/rGO composites containing 5%, 10%, 15%, and 20% of rGO are denoted as $CoSb_2O_6$/rGO_5, $CoSb_2O_6$/rGO_10, $CoSb_2O_6$/rGO_15, and $CoSb_2O_6$/rGO_20 for convenience. X-ray diffraction was used to analyze the material's crystal structure, phase, space group, and crystallite size. Fig. 2(a) compares $CoSb_2O_6$ and $CoSb_2O_6$/rGO composites, which perfectly match the JCPDS (reference) file no. 01-084-2062.[37] All the peaks present in XRD correspond to the Bragg's angle at 19.12°, 21.36°, 27.101°, 33.380°, 34.817°, 38.701°, 39.336°, 43.51°, 53.030°, 55.886°, 59.767°, 63.189°, 66.813°, 67.554°, 73.505°, 80.664°, 83.260°, 86.310°, and 89.566° can be assigned to the (002), (101), (110), (112), (103), (004), (113), (210), (211), (213), (220), (006), (310), (116), (30 223), (206), (323), (008), (226), and (118) planes showing the crystal system of tetragonal structured $CoSb_2O_6$ and $CoSb_2O_6$/rGO composites. It shows a highly crystalline structure with growth oriented along the

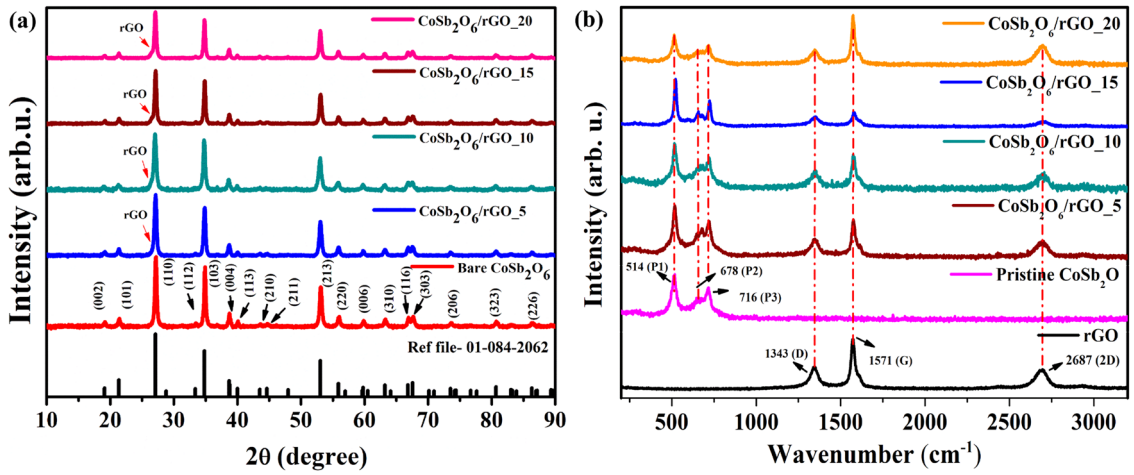


Fig. 2 (a) Comparison of the X-ray diffraction (XRD) patterns of $CoSb_2O_6$ and $CoSb_2O_6$/rGO composites; (b) Raman spectra of rGO, $CoSb_2O_6$, and its rGO composites.

(110) lattice plane and the *P*42/*mnm* space group. To validate the lattice parameters *a*, *b*, and *c*, we have calculated *d*-spacing using Bragg's law as shown in eqn (5):

$$n\lambda = 2d\sin\theta$$

or

$$d = \frac{n\lambda}{2\sin\theta} \quad (5)$$

where $\lambda$ is 1.5406 Å, $\theta$ is the peak position (in radian), $n$ is 1 (order of diffraction), and $d$ is the interplanar spacing (Å). And to calculate the lattice constant, we have used eqn (6), *i.e.*, for the tetragonal phase ($a = b \neq c$):

$$\frac{1}{d^2} = \frac{h^2 + k^2}{a^2} + \frac{l^2}{c^2} \quad (6)$$

From this, we have calculated the *d*-spacing and the lattice constant, and the values are presented inTables S1 and S2 (SI). From these values, we can observe that the calculated values of *a*, *b*, and *c* are approximately equal to the JCPDS file (standard values). The XRD patterns of $CoSb_2O_6$/rGO composites show that all peaks perfectly match with the pristine $CoSb_2O_6$ and JCPDS file, and an additional peak of reduced graphene oxide is observed at 26.77°, confirming the formation of $CoSb_2O_6$/rGO composites. An enlarged image showing a comparison of XRD with the JCPDS file for pristine $CoSb_2O_6$, $CoSb_2O_6$/rGO_5, $CoSb_2O_6$/rGO_10, $CoSb_2O_6$/rGO_15, and $CoSb_2O_6$/rGO_20 is shown in Fig. S2. All XRD patterns perfectly match with the JCPDS file. As the ratio of rGO is increased in $CoSb_2O_6$, the broadening of the peak (at an angle of 27.10°) also increases. The XRD pattern of reduced graphene oxide is shown in Fig. S1 (SI). The crystallite size of cobalt antimony oxide is determined by using eqn (7) (*i.e.*, Scherrer equation):[38]

$$D = (k\lambda)/(\beta\cos\theta) \quad (7)$$

where $D$ is the crystallite size, $\lambda$ is the XRD wavelength (*i.e.*, 0.15 nm for CuKα radiation), $\beta$ is the peak width at half maximum intensity, and $\theta$ is the peak position or Bragg angle. The crystallite size is calculated to be 21.42 nm using the Scherrer equation.

To explore more structural information, Raman spectroscopy was further employed. It is an essential tool for confirming the $CoSb_2O_6$/rGO composite phase, providing information on lattice defects. The Raman spectra of rGO, $CoSb_2O_6$, and its rGO composites are shown in Fig. 2(b). The Raman spectra of GO and rGO are shown in Fig. S3. The graphitic materials exhibit first-order bands at 1347 $cm^{-1}$ and 1343 $cm^{-1}$ (D), and 1570 $cm^{-1}$ and 1571 $cm^{-1}$ (G) for GO and rGO, respectively. rGO shows a moderate defect intensity ($I_D/I_G$), *i.e.*, 0.47, and the corresponding plane crystallite size ($L_a$) is ~40.9 nm (calculated using the Tuinstra–Koenig relation given in eqn (8)), considering partial restoration of the $sp^2$ domain after reduction.[39] In Fig. 2(b), $CoSb_2O_6$ displays three distinct phonon peaks at 514, 678, and 716 $cm^{-1}$, which correspond to the vibrational modes of the cobalt antimony oxide lattice and confirm the formation of the oxide phase. All these oxide modes are present in all composites, indicating that the oxide phase is preserved upon compositing with rGO. In $CoSb_2O_6$/rGO composites, the Raman features of both $CoSb_2O_6$ and rGO are present and show systematic changes with varying rGO loadings (10–15%) (shown in Table S3). The D and G band positions for all composites are nearly constant, but the $I_D/I_G$ ratio and calculated $L_a$ values change with different compositions. From this, we measured the $I_D/I_G$ ratio (Table S3) and calculated the crystallite sizes ($L_a$) using the Tuinstra–Koenig relation (*i.e.*, eqn (8))[40] (at 532 nm excitation) to be 36.26 (GO), 40.89 (rGO), 33.72 (5%), 30.51 (10%), and 26.94 (15%). This trend indicates the introduction of additional defects and distortion in the $sp^2$ lattice, arising from strong interfacial interactions and nucleation of $CoSb_2O_6$ and rGO. The $CoSb_2O_6$/rGO_15 composite exhibits the highest defect density, providing abundant anchoring sites for nanoparticles, increasing the redox activity due to its accessible surface area, and enabling faster electron transfer.

$$L_a\ (\mathrm{nm}) = \frac{2.4 \times 10^{-10}\lambda^4}{(I_D/I_G)} \quad (8)$$

The increasing defect density in the $CoSb_2O_6$/rGO_15 composite sample led to an improved electrochemical performance, consistent with the lower charge transfer resistance and higher specific capacity observed in the electrochemical measurements.

XPS was performed to examine the chemical composition and electronic states of $CoSb_2O_6$ and $CoSb_2O_6$/rGO_15. The high-resolution XPS spectra of Co 2p, Sb 3d, O 1s, and C 1s are shown in Fig. 3(a)–(d). The complete XPS survey spectrum of $CoSb_2O_6$ and $CoSb_2O_6$/rGO_15 is shown in Fig. 2(a). The XPS spectra were deconvoluted using Fityk software, resulting in perfect curve fitting. Fig. 2(b) shows the high-resolution Co 2p spectra of both $CoSb_2O_6$ and $CoSb_2O_6$–15% rGO, which were fitted using a Voigt profile (G : L = 70 : 30) and a Shirley-type background with two doublet peaks at 796.4–796.5 eV and 780.7 eV, corresponding to $2p_{1/2}$ and $2p_{3/2}$, respectively. In addition to these prominent peaks, two satellite peaks are observed at 802.6 eV and 785.95 eV. These satellite peaks are about 5–6 eV higher in binding energy than the prominent peaks, indicating that the electronic state of Co is approaching the +2 oxidation state, which is in good agreement with previously reported literature.[41] The interaction with rGO modifies the electronic structure but does not alter the dominant oxidation state. Comparing the two samples, the Co 2p peaks in the $CoSb_2O_6$/rGO_15 composite show a slight binding energy shift, *i.e.*, ~0.1 to 0.7 eV. This shift indicates an increase in partial electron density around $Co^{2+}$. In addition, the $Co^{2+}$ peaks in the composite become noticeably sharper and more intense, reflecting a reduction in surface defects due to rGO addition, which enhances charge-transfer capability through the conductive rGO framework. In Fig. 2(c), the Sb 3d and O 1s core-level spectra of both pristine $CoSb_2O_6$ and the $CoSb_2O_6$–15% rGO composite were re-deconvoluted to address the overlap between Sb $3d_{5/2}$ and O 1s signals. Two high-resolution Sb 3d peaks are observed at 530.5–530.6 eV and 539.8–540.0 eV, corresponding to the $3d_{5/2}$ and $3d_{3/2}$ states, respectively. Due to the spin–orbit coupling, the energy separation between these two peaks is about 9–9.5 eV, corresponding to the higher number of oxidation states (+5) of antimony (Sb). Additionally, the peak shift in $CoSb_2O_6$/rGO_15 compared to pristine $CoSb_2O_6$ at 540 eV indicates increasing $Sb^{5+}$ character.[42] In $CoSb_2O_6$, minor peaks at 530.35 and 539.82 eV suggested the presence of reduced Sb species ($Sb^{3+}$). The O–C peak at 532.09 eV was assigned to surface-adsorbed species or oxygen vacancies. A broad peak of O 1s in $CoSb_2O_6$/rGO_15 at 530.99 eV suggests overlapping with lattice oxygen, hydroxyl groups, and potentially functional groups from rGO. The XPS data of O 1s are shown in Fig. S4(a) and (b) for both pristine $CoSb_2O_6$ and the $CoSb_2O_6$–15% rGO composite. One peak is observed at 530.59 eV for O 1s, which is closely related to the binding energy of Sb 3d. The XPS peaks for C 1s are shown in Fig. 2(d); the main peak of carbon is observed at 284.09 eV, corresponding to C–C/C=C. Some other peaks are observed at 284.93 eV and 288.15 eV due to the respective functional groups C–OH (carboxylic) and C=O (carbonyl).[43] The dominant $sp^2$ carbon peak reflects the presence of conductive graphene sheets. Meanwhile, the presence of oxygen-functionalized carbon peaks enhances electrolyte diffusion. The SI provides detailed data on XPS in a tabular form (Table S5 for pristine $CoSb_2O_6$ and Table S6 for $CoSb_2O_6$/rGO_15). When comparing the XPS spectra between

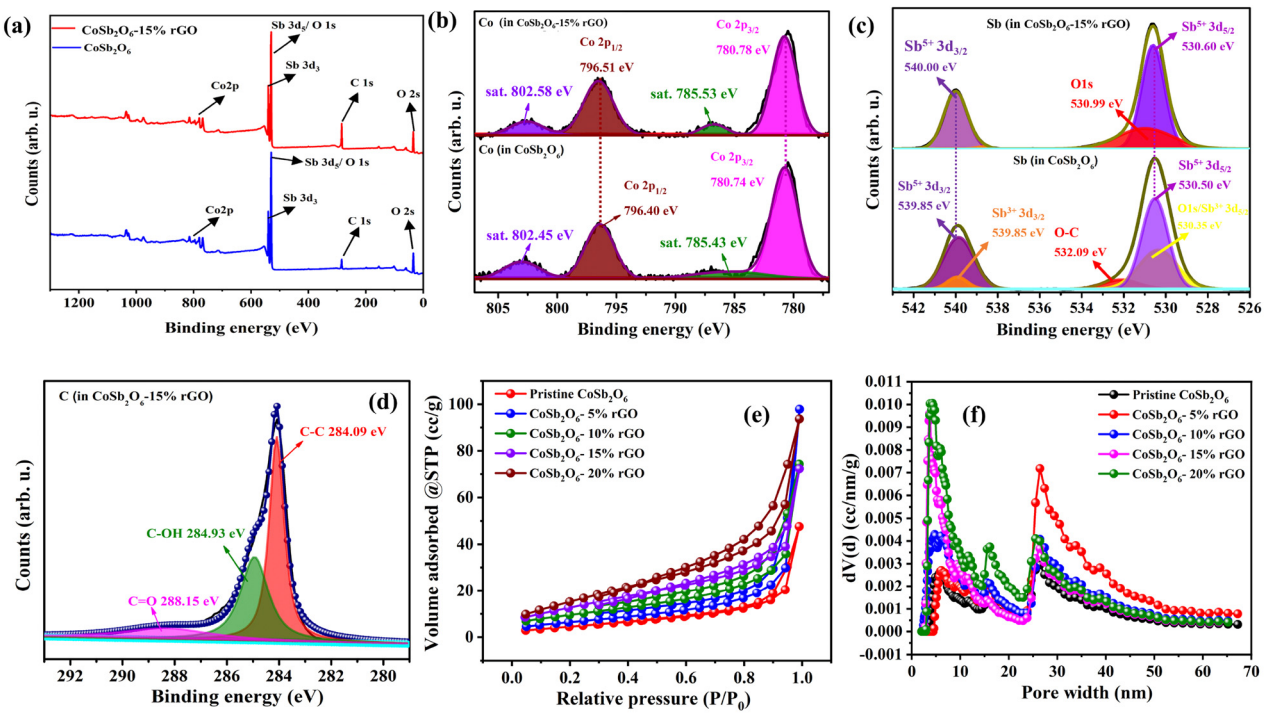


Fig. 3 XPS spectra of both $CoSb_2O_6$ and $CoSb_2O_6$–15% reduced graphene oxide composites: (a) full survey spectrum, (b) Co 2p, (c) Sb 3d, and (d) C 1s. The BET isotherms for (e) $CoSb_2O_6$ and $CoSb_2O_6$/rGO composites. (f) Pore size distribution curves for $CoSb_2O_6$ and $CoSb_2O_6$/rGO composites.

$CoSb_2O_6$ and $CoSb_2O_6$/rGO_15, a minor chemical peak shift is present in $CoSb_2O_6$–15% rGO due to the addition of rGO to $CoSb_2O_6$.

To analyse the porosity (pore diameter and pore volume), the surface area of the nanoparticles was measured using $N_2$ adsorption and desorption isotherms (BET isotherms). Fig. 3(e) shows that all samples exhibit type IV isotherms with noticeable hysteresis loops (H3). The surface area of $CoSb_2O_6$/rGO_15 was determined to be 50 $m^2$ $g^{-1}$. Fig. 3(e) compares the BET isotherms of cobalt antimony oxide and its rGO composites. A comparison of the specific surface area, pore diameter, and pore volume is presented in Table 1. As shown in Table 1, when the weight percentage of rGO increases, the specific surface area also increases from 16.671 $m^2$ $g^{-1}$ for pristine $CoSb_2O_6$ to 61.804 $m^2$ $g^{-1}$ for 20% (by wt%) rGO in $CoSb_2O_6$. The maximum pore diameter ranges between 3 and 4 nm, indicating a mesoporous structure of cobalt antimony oxide and its rGO composites. This structure offers a large number of electrochemically active sites, thereby facilitating rapid ion absorption and faster charge transfer at the electrode–electrolyte interface.[44] The highest pore diameter of $CoSb_2O_6$/rGO_15 is 3.82 nm, which significantly improves the electrochemical charge storage performance. After the addition of rGO, the surface area and porosity increase, which is favorable for electrochemical performance. Subsequently, the pore-size distribution graph of the synthesized materials is presented in Fig. 3(f) for further clarification. These graphs show the presence of mesoporous particles in their structure. As the percentage of reduced graphene oxide increases, the pore size also increases. Here, the pore size distribution of $CoSb_2O_6$/rGO_15 and $CoSb_2O_6$/rGO_20 is almost the same, even with a 5% increase in rGO, suggesting that the distribution remains the same. Therefore, the improved specific capacitance value can be attributed to the increased percentage of rGO, offering a large surface area.[45]

Table 1 Physical properties of pristine $CoSb_2O_6$ and its reduced graphene oxide (rGO) composites with different rGO contents

| Sample name | Surface area ($m^2$ $g^{-1}$) | Pore diameter (nm) | Pore volume (CC $g^{-1}$) |
|---|---|---|---|
| $CoSb_2O_6$ | 16.67 | 3.05 | 0.0714 |
| $CoSb_2O_6$/rGO_5 | 24.20 | 3.40 | 0.1475 |
| $CoSb_2O_6$/rGO_10 | 35.24 | 3.39 | 0.1062 |
| $CoSb_2O_6$/rGO_15 | 50.00 | 3.82 | 0.1030 |
| $CoSb_2O_6$/rGO_20 | 61.80 | 3.38 | 0.1291 |

Field emission scanning electron microscopy was used to examine the surface morphology of $CoSb_2O_6$ and its rGO composites. Fig. 4 shows the micrographs of pristine $CoSb_2O_6$ and $CoSb_2O_6$/rGO_15. Fig. 4(a)–(c) shows the micrographs of $CoSb_2O_6$ at different magnifications and scales (*i.e.*, 1 μm, 200 nm, and 200 nm). In these micrographs, we can observe the uniform formation of nanoparticles. Some of the nanoparticles show a larger size, which is due to the agglomeration effect between the nearby interconnected nanoparticles. Fig. 4(d)–(f) shows the micrographs of the $CoSb_2O_6$/rGO_15 composite at different magnifications and scales (*i.e.*, 1 μm, 200 nm, and 200 nm), where the yellow circle indicates the rGO sheet in the composite and the red circle indicates the cobalt antimony decorated with the reduced graphene oxide composite. From Fig. 4(d)–(f), we can observe that all nanoparticles are uniformly distributed on the surface of reduced graphene oxide. Reduced graphene oxide behaves as a conductive substrate for the cobalt antimony oxide particles, which enhances the electrochemical performance.[46] Fig. S5(a)–(c) of the SI show

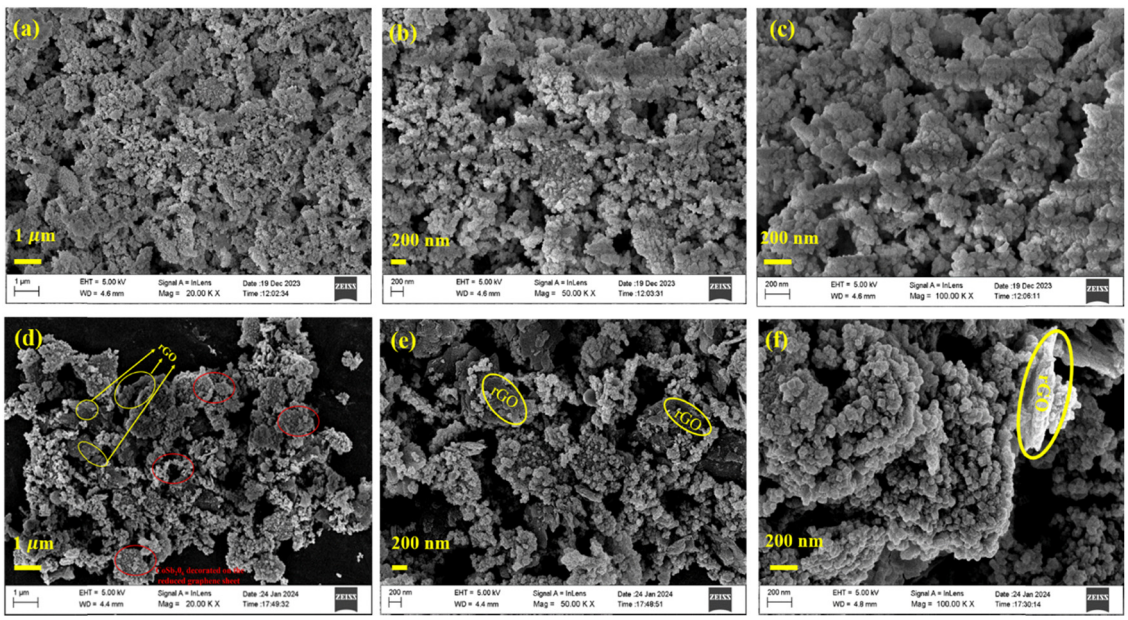


Fig. 4 FE-SEM micrographs of $CoSb_2O_6$ at different scales: (a) 1 μm, (b) 200 nm, and (c) 200 nm. FE-SEM micrographs of the $CoSb_2O_6$/rGO_15 composite at different magnifications: (d) 1 μm, (e) 200 nm, and (f) 200 nm.

the SEM images of all other composites. The micrographs of $CoSb_2O_6$/rGO_5, $CoSb_2O_6$/rGO_10, and $CoSb_2O_6$/rGO_20 taken at a 50 KX magnification, shown in Fig. S5(a)–(c), demonstrate a uniform distribution of the reduced graphene oxide sheets. Energy dispersive spectroscopy (EDS) was used to determine the elemental composition. Fig. S6(a)–(e) shows cobalt antimony oxide with the presence of all elements: Co, Sb, and O. The measured Co : Sb ratio is ~1 : 2, which agrees with the composition of trirutile type $CoSb_2O_6$. A minor deviation from the ideal 1 : 2 : 6 stoichiometry in the oxygen content is expected because the EDS instrument shows limited sensitivity to the lighter elements, which tends to underestimate O relative to Co or Sb. Fig. S7(A)–(D) shows the elemental composition of $CoSb_2O_6$/rGO_5, $CoSb_2O_6$/rGO_10, $CoSb_2O_6$/rGO_15, and $CoSb_2O_6$/rGO_20, respectively. Fig. S7[A(a)–(f)], [B(a)–(f)], [C(a)–(f)], and [D(a)–(f)] shows the elemental composition of $CoSb_2O_6$/rGO_5, $CoSb_2O_6$/rGO_10, $CoSb_2O_6$/rGO_15, and $CoSb_2O_6$/rGO_20, respectively.

HR-TEM images are presented in Fig. 5 to further understand the structure and morphology. Fig. 5(a)–(e) shows the morphology of $CoSb_2O_6$/rGO_15 at different scales from 500 to 5 nm. In Fig. 5(e), the *d*-spacing is approximately 0.32 nm, which corresponds to the (110) lattice plane of $CoSb_2O_6$, and the inset shows the selected area electron diffraction pattern, which reveals the polycrystalline nature of $CoSb_2O_6$/rGO_15. Fig. 5(f) shows the EDS image of $CoSb_2O_6$/rGO_15 at a scale of 500 nm, which reveals the presence of all elements in the layers.[47] Fig. S8 shows the HR-TEM images, SAED pattern, and the bare cobalt antimony oxide's particle size. Fig. S8(a)–(f) shows the morphology of $CoSb_2O_6$ at different scales, from 200 nm to 5 nm. The inset of Fig. S8(a) shows the histogram of the particle size distribution corresponding to the 200 nm image, with the average particle size, measured from the histogram, being 36.61 nm. The HR-TEM image in Fig. S8(e) shows *d*-spacings of 0.3 nm and 0.46 nm, corresponding to the (111) and (101) planes of $CoSb_2O_6$, respectively. This interplanar spacing showed good agreement with the XRD data. Fig. S8(f) presents the SAED pattern for cobalt antimony oxide. The bright points in the SAED pattern indicate the highly crystalline structure of $CoSb_2O_6$. The concentric rings of nanoparticles correspond to the (101), (110), (112), (004), (213), and (310) planes of $CoSb_2O_6$, which are in good agreement with the XRD pattern. Additionally, the EDS analysis conducted during HR-TEM for $CoSb_2O_6$ and $CoSb_2O_6$/rGO_15, shown in Fig. S9(a)–(f) and Fig. 5(g)–(k), confirms the presence of all the desired elements and compositions. The above analysis confirms the successful formation of pure $CoSb_2O_6$ and $CoSb_2O_6$/rGO_15

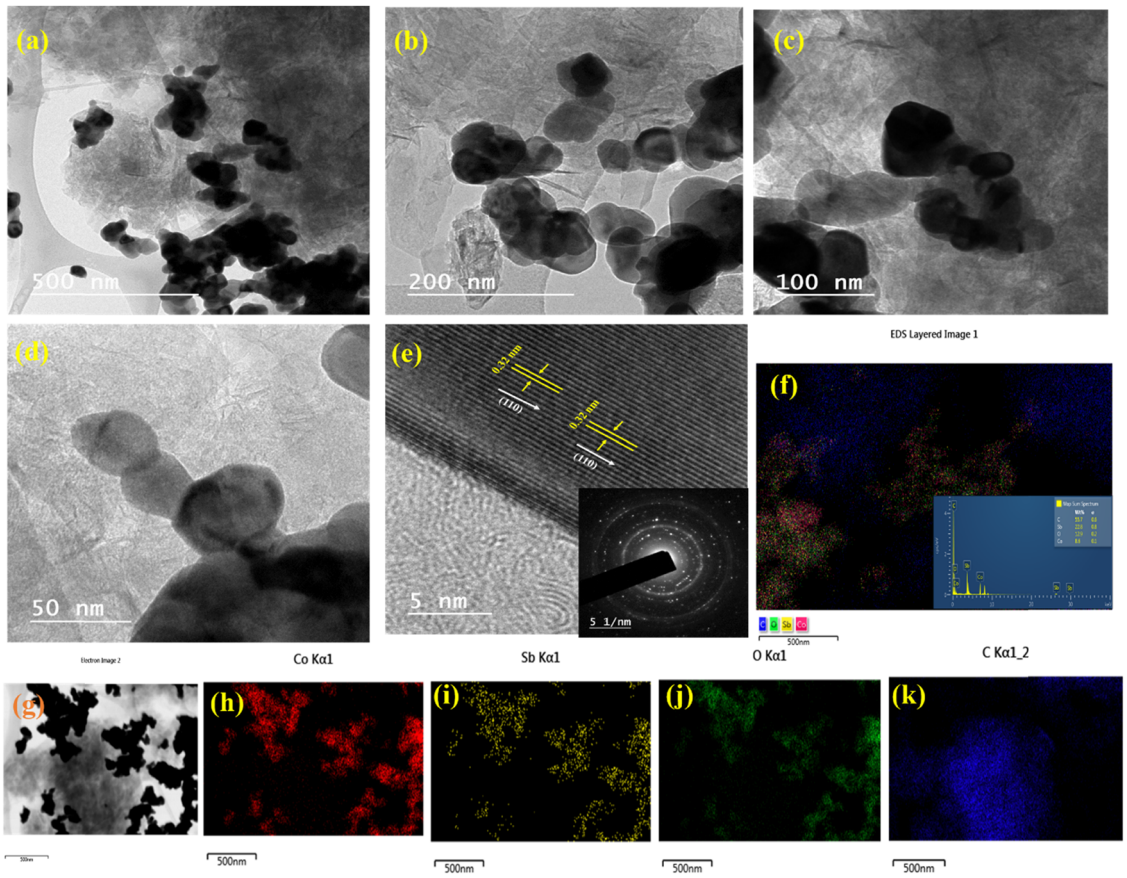


Fig. 5 HR-TEM micrographs of $CoSb_2O_6$/rGO_15 at different magnifications: (a) 500 nm, (b) 200 nm, (c) 100 nm, (d) 50 nm, and (e) 5 nm; inset: SAED pattern of $CoSb_2O_6$/rGO_15. (f) Layered EDS image at a scale of 500 nm for $CoSb_2O_6$/rGO_15. (g) Electronic image of $CoSb_2O_6$/rGO_15 showing the presence of (h) cobalt, (i) antimony, (j) oxygen, and (k) carbon.

composite nanostructures. The structure is nearly uniform in shape and size, making it highly suitable for supercapacitor applications.

### 3.2 Electrochemical analysis

To understand the electrochemical kinetics of cobalt antimony oxide and its rGO composite (at different weight percentages), we performed cyclic voltammetry (CV), galvanostatic charge–discharge cycling (GCD), and electrochemical impedance spectroscopy (EIS). First, we conducted three-electrode measurements for $CoSb_2O_6$ and all its rGO composites to enable systematic comparisons. The potential window for all CV curves was 0–1.1 V *vs.* Ag/AgCl in 1 M aqueous $Na_2SO_4$ electrolyte. Fig. 6(a) presents the CV comparison plot for rGO, pristine $CoSb_2O_6$, and $CoSb_2O_6$/rGO_15 (which shows the best performance among all composite materials) at 100 mV $s^{-1}$. This plot shows that rGO displays a quasi-rectangular shape, revealing the material's capacitive or EDLC nature.[48] For pristine $CoSb_2O_6$, the capacitance originated from the pseudocapacitance mechanism. The addition of 15% rGO to pristine $CoSb_2O_6$ leads to an increase in both area and peak current, resulting from the synergistic effect of rGO, which provides a more conductive surface for pristine $CoSb_2O_6$ nanoparticles.[49] The cyclic voltammetry curve of $CoSb_2O_6$/rGO_15 is illustrated in Fig. 6(b) at various scan rates ranging from 5 mV $s^{-1}$ to 100 mV $s^{-1}$. The increase in the scan rate influences the peak current and potential response. The shape of

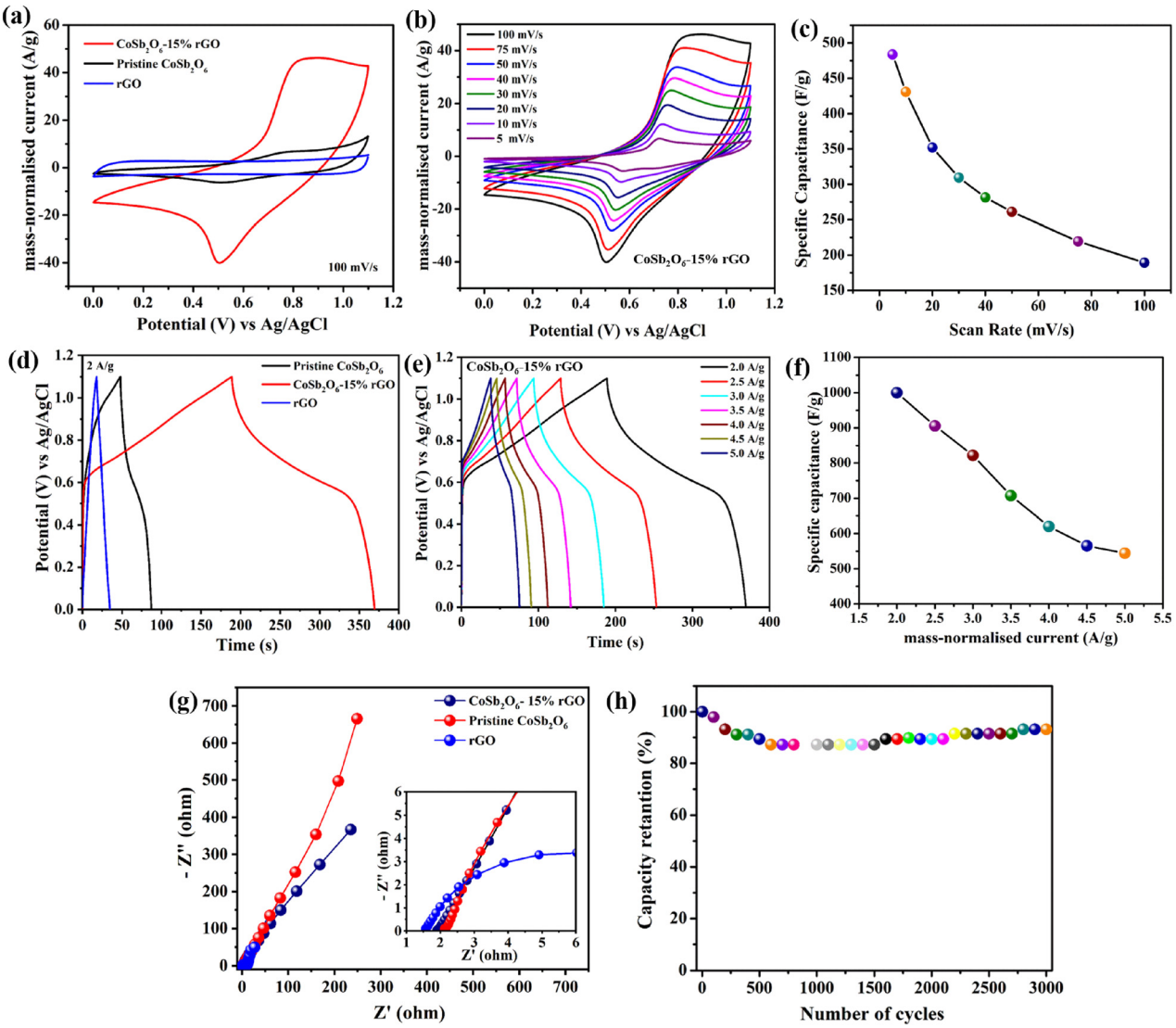


Fig. 6 Electrochemical analysis of the prepared $CoSb_2O_6$ and $CoSb_2O_6$/rGO_15 composite: (a) comparative specific capacitance profiles for rGO, $CoSb_2O_6$, and the $CoSb_2O_6$/rGO_15 composite, (b) CV plots of the $CoSb_2O_6$/rGO_15 composite electrode at various scan rates, (c) effect of scan rate on the specific capacitance of the $CoSb_2O_6$/rGO_15 composite electrode, (d) comparative charge–discharge profiles of rGO, $CoSb_2O_6$, and the $CoSb_2O_6$/rGO_15 composite at a mass-normalised current of 2 A $g^{-1}$, (e) CD plots of the $CoSb_2O_6$/rGO_15 composite at different applied mass-normalised current values, (f) effect of different applied current values on the specific capacitance of the $CoSb_2O_6$/rGO_15 composite, (g) comparison of Nyquist plots for rGO, $CoSb_2O_6$ and the $CoSb_2O_6$/rGO_15 composite electrode, with the inset showing an enlarged portion of the plots, and (h) cyclic stability of the $CoSb_2O_6$/rGO_15 composite electrode over 3000 cycles.

the CV curves shows oxidation and reduction peaks, which clarify the redox behavior of $CoSb_2O_6$/rGO_15, indicating the pseudocapacitive behavior of the electrode material.[50] At high scan rates, we observe that the peak shape is less sharp compared to low scan rates, indicating the presence of high diffusive resistance. Conversely, the diffusive resistance decreases at lower scan rates, resulting in the occurrence of anodic and cathodic peaks at nearly identical potentials. This is because the longer time to complete the cycle allows for greater interaction between the electrode and electrolytic ions, reflecting the electrochemically reversible nature of the electrode. From Fig. 6(c), which displays the plot of scan rate *vs.* specific capacitance, we calculate a maximum capacitance of 483.52 F $g^{-1}$ at a scan rate of 5 mV $s^{-1}$ for $CoSb_2O_6$/rGO_15. This value is four times greater than the specific capacitance value of 115.2 F $g^{-1}$ for pristine $CoSb_2O_6$, indicating that rGO addition enhances the material's electrochemical performance.[51] The comparison of cyclic voltammetry curves for pristine $CoSb_2O_6$, $CoSb_2O_6$/rGO_5, $CoSb_2O_6$/rGO_10, $CoSb_2O_6$/rGO_15, and $CoSb_2O_6$/rGO_20 is shown in Fig. S11. Fig. S11(a)–(e) shows the CV plots of pristine $CoSb_2O_6$, $CoSb_2O_6$/rGO_5, $CoSb_2O_6$/rGO_10, $CoSb_2O_6$/rGO_15, and $CoSb_2O_6$/rGO_20, respectively. To calculate the contribution of nickel (Ni) foam to the capacitance, the electrochemical response of bare Ni foam is presented in Fig. S10 of the SI. The bare Ni foam shows a negligible contribution to the tested potential window, confirming that its influence on the measured capacitance value is less.

We can observe that the peak current response also increases as the weight percentage of rGO increases. This increase is due to the addition of rGO, which enhances the charge transfer at the electrode and electrolyte interface and provides a shorter diffusion length for the interaction of electrolytic ions. However, from Fig. S11(d) and (e), we see that, after adding an additional 5% rGO, the current response does not significantly increase and remains similar to that observed with the addition of 15% $CoSb_2O_6$. Furthermore, there is no significant increase in capacitance.[52] The area under the curve and shape of all CV tests exhibit symmetric curves, and as the weight percentage increases, the area under the curve also expands. The reason behind this improvement with 20% rGO arises from the EDLC contribution, not from the faradaic contribution. rGO mainly contributes to the electric double-layer capacitance, while $CoSb_2O_6$ contributes to the pseudocapacitance. Pseudocapacitance sites saturate at 15%; an additional 5% rGO improves only the EDLC contribution, resulting in a smaller capacitance gain. Another reason is that increasing the rGO content reduces the relative mass fraction of $CoSb_2O_6$, which carries the majority of the pseudocapacitive charge. We observe a smaller increase in specific capacitance when adding 5% additional rGO to the EDLC (15% behavior). This combined effect explains why rGO shows very little increase in the capacitance relative to 15% rGO. From this cyclic voltammetry test, we can conclude that $CoSb_2O_6$/rGO_15 shows better electrochemical performance.

The galvanostatic charge–discharge cycling for pristine $CoSb_2O_6$ and its rGO composites was performed in a potential window of 0–1.1 V *vs.* Ag/AgCl using the same electrolyte. Fig. 6(d) shows the comparative GCD cycle for rGO, pristine $CoSb_2O_6$, and $CoSb_2O_6$/rGO_15 at a mass-normalised current value of 2 A $g^{-1}$. Fig. 5(d) shows that rGO shows a triangular-shaped charge–discharge curve. In contrast, pristine $CoSb_2O_6$ deviates from the generally triangular shape of EDLC behavior, which is attributed to the surface diffusion control mechanism.[53] However, the $CoSb_2O_6$/rGO_15 curve shows clear plateaus representing the electrode material's more diffusion-controlled or pseudocapacitive behavior. A detailed GCD study of $CoSb_2O_6$/rGO_15 is presented in Fig. 6(e) at various constant current values ranging from 2 A $g^{-1}$ to 5 A $g^{-1}$. This plot reveals a symmetrical and reversible curve for all current values.[54] As the current value increases, the time taken to complete the cycle decreases, indicating that a large amount of charge is being transferred at low current values as the interaction time increases. At high current values, ions from the electrolyte do not get enough time to interact, and the inactive diffusion reaction activity is attributed to the incomplete coverage of the electrode surface, resulting in a lower capacitance value. From this analysis, we calculate the specific capacitance at different values, as shown in Fig. 6(f). The high capacitance value at 2 A $g^{-1}$ is 1000 F $g^{-1}$, varying as follows: 1000 F $g^{-1}$, 821.7 F $g^{-1}$, 707.07 F $g^{-1}$, 620.15 F $g^{-1}$, 565.33 F $g^{-1}$, and 544.07 F $g^{-1}$ at mass-normalised current values of 2 A $g^{-1}$, 2.5 A $g^{-1}$, 3 A $g^{-1}$, 3.5 A $g^{-1}$, 4 A $g^{-1}$, 4.5 A $g^{-1}$, and 5 A $g^{-1}$, respectively. Given that the mass loading is 1 mg, a maximum specific capacitance value of 1000 F $g^{-1}$ occurs at a mass-normalised current value of 2 A $g^{-1}$, which is approximately 5-fold higher than that of pristine $CoSb_2O_6$ (*i.e.*, 195.5 F $g^{-1}$ at a mass-normalised current value of 2 A $g^{-1}$). The detailed study of all electrode materials is shown in Fig. S12(a)–(f). Fig. S12(a)–(e) presents the GCD curves of $CoSb_2O_6$, $CoSb_2O_6$/rGO_5, $CoSb_2O_6$/rGO_10, $CoSb_2O_6$/rGO_15, and $CoSb_2O_6$/rGO_20, respectively. Pristine $CoSb_2O_6$ does not exhibit a proper EDLC triangular shape and shows some deviation. However, with increasing the percentage of rGO in pristine $CoSb_2O_6$, the time taken to complete the cycle increases and the shape of the curve changes to reflect a more diffusive contribution.[55] It is observed that the presence of 20% rGO leads to an increased cycle time compared to the 15% rGO electrode. However, after increasing the rGO content to 20% (*i.e.*, 15% + 5% more), the additional impact of rGO beyond 15% is negligible. As illustrated in Fig. S12(f), the comparison of specific capacitance at a current value of 2 mA reveals that the increase of specific capacitance for 5%, 10%, and 15% rGO is almost symmetrical. Nevertheless, the composite with 20% rGO shows increased specific capacitance, which is, however, not significant. Therefore, the increase beyond 15% may decrease the performance due to increased resistance across the reduced graphene oxide layers. From this analysis, we conclude that the presence of 15% rGO in pristine $CoSb_2O_6$ leads to a higher capacitance value of 1000 F $g^{-1}$ at a mass-normalised current value of 2 A $g^{-1}$. This enhancement is attributed to the synergistic effect of the EDLC charge storage of rGO and the pseudocapacitive charge storage mechanism of $CoSb_2O_6$, demonstrating that rGO addition enhances the material properties and electrochemical reaction pathways. We have calculated the specific capacity from the GCD curves of $CoSb_2O_6$ and its rGO composite, as shown in Fig. S13 (and the calculated values are

presented in Table S6). The maximum specific capacity of $CoSb_2O_6$/rGO_15 is 1100 C $g^{-1}$ at an applied mass-normalised current of 2 A $g^{-1}$, whereas the pristine $CoSb_2O_6$ electrode exhibits a specific capacity of 215.05 C $g^{-1}$ under the same conditions.

Electrochemical impedance spectroscopy (EIS) is a crucial technique for studying the electrochemical kinetics of supercapacitive electrode materials. Fig. 6(g) presents the Nyquist plot, with a zoomed-in view covering the frequency range of 100 kHz–0.1 Hz for rGO, $CoSb_2O_6$, and $CoSb_2O_6$/rGO_15. From this plot, we analyze the electrode material's electrolytic or solution resistance ($R_s$), which appears in the high-frequency region. The diameter of the semicircle in the high-frequency region represents the charge transfer resistance ($R_{ct}$) at the electrode–electrolyte interface. In contrast, the line in the low-frequency region corresponds to the Warburg region.[56] For pristine $CoSb_2O_6$, the solution resistance is 2.12 Ω and the charge transfer resistance is 3.11 Ω. To improve performance and reduce resistance, we developed a composite with rGO that exhibits the lowest solution resistance of 1.42 Ω, significantly lower than that of pristine $CoSb_2O_6$. Adding rGO enhances the performance of the $CoSb_2O_6$/rGO_15 composite, which has a solution resistance of 1.09 Ω. The semicircle's diameter near the real axis shows that $CoSb_2O_6$/rGO_15 has a lower $R_{ct}$ value of ~2.58 Ω, indicating faster charge transfer at the electrode–electrolyte interface. The lower resistance in the composite material corresponds to improved electrochemical performance, contributing to higher specific capacitance. The EIS fitted parameters are presented in Table S9 of the SI. A Bode plot was generated to examine the deviation from the ideal capacitor angle (−90°) and the charge storage mechanism.[57] The characteristic frequency, $f_0$, for the phase angle −45° marks the point at which resistive and capacitive impedance are equal. $f_0$ represents a time constant, $\tau_0 = \frac{1}{2\pi f_0}$, which defines how fast the device can charge and discharge. From Fig. S14, the phase angle for the $CoSb_2O_6$/rGO_15 composite electrode is −45.97°, indicating a predominant pseudocapacitive or diffusive charge storage behavior. For this Bode plot, the corresponding time constant is 0.836 ms. This lower time constant confirms excellent rate capability and fast ion transfer. Additionally, cyclic stability and capacity retention were tested over 3000 cycles. Fig. 6(h) shows that the $CoSb_2O_6$/rGO_15 composite retains 93.18% of its capacity after 3000 cycles.

To quantitatively understand the charge storage process, the Trasatti plot was analyzed for both pristine $CoSb_2O_6$ and $CoSb_2O_6$/rGO_15, which allows us to assess both capacitive and pseudocapacitive contributions.[58] Fig. S15(a) and (c) shows the $y$-intercept of the linear fit of $1/C_p$ *vs.* $v^{1/2}$, while Fig. S15(b) and (d) presents the $y$-intercept of the linear fit of $C_{sp}$ *vs.* $v^{-1/2}$ for pristine $CoSb_2O_6$ and the $CoSb_2O_6$/rGO_15 composite electrode. Then, we analyzed the overall percentage of capacitive and pseudocapacitive contributions. Fig. S15(e) shows that pristine $CoSb_2O_6$ exhibits an EDLC contribution of 6.98%, while the pseudocapacitive contribution is 93.02%. After adding rGO into $CoSb_2O_6$, the EDLC contribution increases to 15.08%, while the pseudocapacitive contribution decreases to 84.92%, facilitating faster charge transfer. The large surface area of rGO allows more ions to interact with the electrode material, enhancing storage performance.

We have employed the Dunn method to distinguish between the capacitive and pseudocapacitive effects.[59] This helps clarify which reaction dominates in the respective electrode materials. For a quantitative description of both capacitive and diffusive control effects, we calculated the $b$-value using the following equation:

$$i_p = av^b \quad (9)$$

$$\log(i_p) = b\log(v) + \log a \quad (10)$$

Here, $i_p$ is the peak current, $v$ is the scan rate, and $a$ and $b$ are constants. Plots of $\log(v)$ *vs.* $\log(i)$ for pristine $CoSb_2O_6$ and $CoSb_2O_6$/rGO_15 are shown in Fig. S16(a) and (b). The cathodic and anodic peak current values from the CV plot yielded $b$-values of 0.57 for the cathodic peak and 0.73 for the anodic peak for pristine $CoSb_2O_6$, suggesting a mixed mechanism of capacitive and diffusive contributions. A $b$-value near 1 suggests a capacitive contribution, while a $b$-value close to 0.5 indicates a diffusive contribution, with values between 0.5 and 1 representing pseudocapacitive contributions.[60]

Similarly, for $CoSb_2O_6$/rGO_15, the $b$-values were approximately 0.66 for the cathodic peak and 0.65 for the anodic peak, indicating that adding rGO reduces the resistance and enhances the charge transfer characteristics. The following equation was used to determine the respective contributions from both processes:

$$i(v) = k_1 v = k_2 v^{1/2} \quad (11)$$

In this equation, $k_1 v$ represents the capacitive effect, and $k_2 v^{1/2}$ represents the diffusive effect, where $k_1$ and $k_2$ are constants. Fig. S17(a) shows the capacitive and diffusive contributions to the CV curve at a scan rate of 5 mV $s^{-1}$, where the green part indicates the capacitive contribution and the blue part indicates the diffusive contribution. Fig. S17(b) displays the contributions for $CoSb_2O_6$/rGO_15. The capacitive contribution remains dominant in pristine $CoSb_2O_6$, and the blue section indicates a minor diffusive contribution. This matches well with the Trasatti plot results. Fig. S17(c) and (d) shows the percentage contributions for $CoSb_2O_6$ and $CoSb_2O_6$/rGO_15 at three different scan rates (5 mV $s^{-1}$, 10 mV $s^{-1}$, and 20 mV $s^{-1}$). As the scan rate increases, the capacitive contribution also increases due to the rapid reaction at the electrode surface. These findings are consistent with the results from the Trasatti plot. The quantitative analysis confirms the good rate performance of $CoSb_2O_6$/rGO_15. The pseudocapacitive contribution dominates due to its excellent rate capability and rapid redox reaction. After conducting all experimental and quantitative analyses, we conclude that $CoSb_2O_6$/rGO_15 exhibits superior supercapacitive performance and can be utilized in supercapacitor device applications.

We conducted two-electrode measurements on the $CoSb_2O_6$/rGO_15 composite symmetric supercapacitive device. The photographic image of the symmetric supercapacitor device is shown in Fig. S18. To assess the electrochemical behavior of the

device, we performed CV, CD, and EIS measurements. Fig. 7(a) shows the CV measurement of symmetric devices at different scan rates. Particularly at higher scan rates, the CV curves show sharp redox peaks, signifying that redox behavior plays a crucial role in determining the capacitance of the symmetric device.[61,62] Even at high potential sweep rates, consistent findings are observed at low to high scan rates, indicating excellent reversibility. Fig. 7(b) shows the GCD curve for 10 continuous cycles at a mass-normalised current value of 2.5 A $g^{-1}$. Fig. 7(c) shows the GCD plot for the symmetric device at different current densities, ranging from 1 A $g^{-1}$ to 5 A $g^{-1}$. We calculated the capacitance from these data, revealing remarkable output values for the device. The specific capacitance at different mass-normalised current values is presented in Fig. 7(d), with a maximum capacitance of 227.79 F $g^{-1}$ recorded at 1 A $g^{-1}$. EIS was performed in the frequency range of 100 kHz to 0.1 Hz to further understand the device's chemical kinetics, as shown in Fig. 7(e). The calculated solution resistance ($R_s$) is 1.02 Ω, and the charge transfer resistance ($R_{ct}$) is 2.25 Ω. These low values of $R_s$ and $R_{ct}$ confirm the excellent performance of the symmetric device. Additionally, the Bode plot, displayed in Fig. 7(f), shows a phase angle of approximately −64.415°, indicating both EDLC and pseudocapacitive contributions, and for the symmetric device, the calculated response time $\tau_0$ is 0.439 ms. A lower time response for the device indicates faster ion transport and faster charge transportation through the device. To quantify the specific energy and power, the Ragone plot, in Fig. 7(g), has been generated, showing a maximum energy density of 38.28 Wh $kg^{-1}$

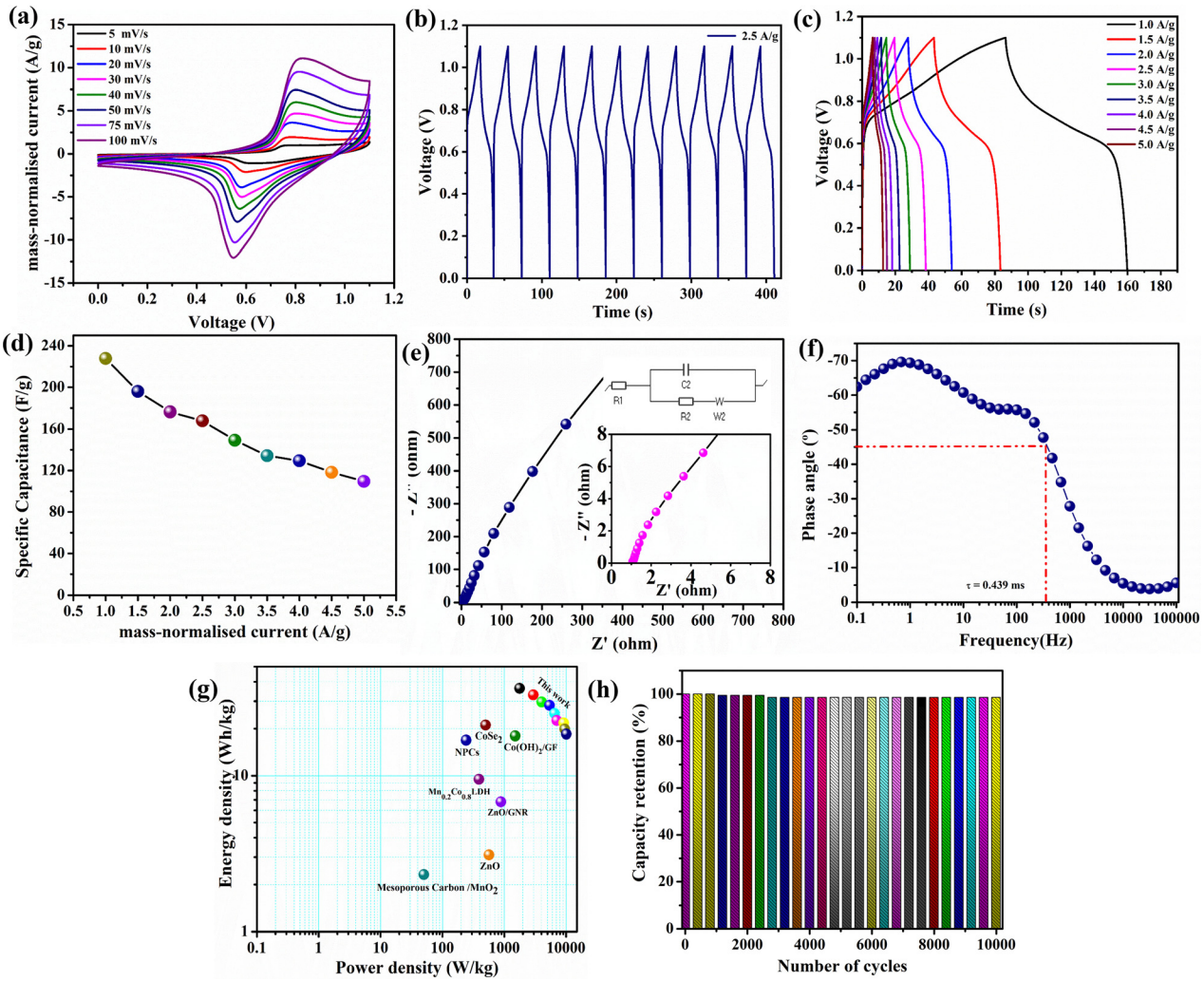


Fig. 7 Electrochemical analysis of the $CoSb_2O_6$/rGO_15//$CoSb_2O_6$/rGO_15 composite symmetric cell device. (a) Cyclic voltammetry profile of the $CoSb_2O_6$/rGO_15 composite symmetric cell device at various scan rates of 5–100 mV $s^{-1}$. (b) First ten charge–discharge cycles at a mass-normalised current of 2.5 A $g^{-1}$. (c) Charge–discharge cycles of the $CoSb_2O_6$/rGO_15 composite symmetric cell device at different mass-normalised current value of 1–5 A $g^{-1}$. (d) Effect of applied current on the specific capacitance of the $CoSb_2O_6$/rGO_15 composite symmetric cell device. (e) Nyquist plot of the $CoSb_2O_6$/rGO_15 composite symmetric cell device in the frequency range of 0.1 Hz to 100 kHz, with the inset showing the equivalent circuit for this plot. (f) Bode plot for the $CoSb_2O_6$/rGO_15 composite symmetric cell device. (g) The Ragone plots showing the performance of the $CoSb_2O_6$/rGO_15 composite symmetric cell device. (h) Cyclic stability of the $CoSb_2O_6$/rGO_15 composite symmetric cell device over 10 000 cycles.

with a corresponding power density of 1837.44 W $kg^{-1}$ and a maximum power density of 10 082.19 W $kg^{-1}$. The Ragone plot indicates the high specific capacitance of the $CoSb_2O_6$/rGO_15 composite symmetric supercapacitive device. It shows a comparison with the performance of other SSD configurations such as the $Mn_{0.2}Co_{0.8}$ LDH (9.5 Wh $kg^{-1}$),[63] $CoSe_2$ (21.1 Wh $kg^{-1}$),[64] $Co(OH)_2$/GF (18 Wh $kg^{-1}$),[65] mesoporous carbon/$MnO_2$ (2.32 Wh $kg^{-1}$),[66] ZnO (3.1 Wh $kg^{-1}$),[67] ZnO/GNR (6.8 Wh $kg^{-1}$),[67] and NPCs (16.9 Wh $kg^{-1}$).[68] A 10 000-cycle test was conducted at a mass-normalised current of 5 A $g^{-1}$ to measure the electrode's stability, as shown in Fig. 7(h). The results indicate a capacity retention of 98.54% after 10 000 cycles. For this cyclic stability, the coulombic efficiency remained close to 100% throughout the 10 000 cycles, as shown in Fig. S19, confirming the stability and absence of parasitic side reactions. For further clarification, Fig. S20 compares the first ten cycles with the last ten cycles, which reveals no substantial difference, affirming the device's exceptional stability. For the reproducibility analysis of the symmetric $CoSb_2O_6$/rGO_15 device based on five different fabricated cells, we present this analysis graph in Fig. S21 of the SI with the corresponding error bars (±SD). The standard deviation across the five devices was found to be 1.258, indicating very small device-to-device variations.

### 3.3 Theoretical analysis

**3.3.1 Structure and electronic properties.** $CoSb_2O_6$ features a well-defined tetragonal crystal structure. The DFT optimized structure of $CoSb_2O_6$ has lattice parameters of $a = b = 4.711$ Å, $c = 10.496$ Å, $\alpha = \gamma = 90$, and $\beta = 116.627$ and the *P*42/*mnm* space group, which aligns with our experimental values of $a = b = 4.6495$ and $c = 9.2763$ as well as the reported experimental values of $a = b = 4.6495$ Å and $c = 9.2763$ Å.[69] From the optimized bulk structure of $CoSb_2O_6$, we have modelled a supercell for the surface of the (110) lattice plane, which exhibited an intense peak in XRD. The optimized structure of the $CoSb_2O_6$(110) surface is depicted in Fig. 8(a). We have used this (110) surface of $CoSb_2O_6$ for further calculations. Afterwards, a composite layer of $CoSb_2O_6$ with reduced graphene oxide (rGO) was designed from the optimized structures of the (110) surface of $CoSb_2O_6$ and rGO, with a minimum separation of 2 Å between layers and an insignificant lattice mismatch. Fig. 8(b) shows the optimized structure of the $CoSb_2O_6$/rGO composite. The calculated binding energy for rGO on $CoSb_2O_6$ is −0.03 eV per atom, which is small, and hence rGO will be mostly connected to $CoSb_2O_6$ *via* van der Waals interactions.

**3.3.2 Orbital interaction and charge transfer.** To study the orbital interaction between $CoSb_2O_6$ and rGO, we have plotted

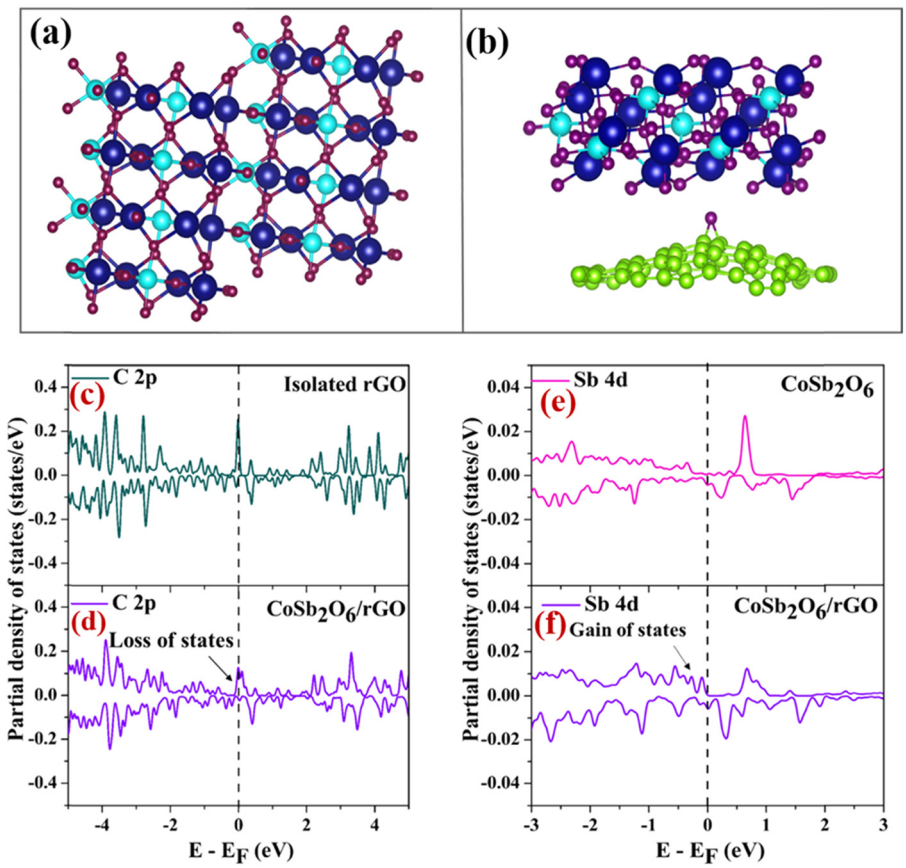


Fig. 8 (a) and (b) Optimised structures of the (110) surface of $CoSb_2O_6$ and $CoSb_2O_6$/rGO, respectively. The blue, cyan, purple, and green spheres represent Sb, Co, O, and C atoms. (c) and (d) Partial density of states plots for the C 2p orbital of isolated rGO and the $CoSb_2O_6$/rGO composite, respectively. (e) and (f) Partial density of states plots for the Sb 4d orbital of the (110) surface of $CoSb_2O_6$ and the $CoSb_2O_6$/rGO composite, respectively. The dotted line drawn vertically at 0 eV on the *x*-axis represents the Fermi level.

the partial density of states (PDOS) for the C 2p orbital and the Sb 4d orbital of rGO and $COSb_2O_6$, respectively. Fig. 8(c) and (d) shows a decrease in the density of states near the Fermi level for the C 2p orbital of $CoSb_2O_6$/rGO than isolated rGO. In contrast, Fig. 8(e) and (f) shows an increase in the density of states near the Fermi level for the Sb 4d orbital of $CoSb_2O_6$/rGO than pristine $CoSb_2O_6$. From this observation, the interaction between $CoSb_2O_6$ and $CoSb_2O_6$/rGO can be attributed to the charge transfer from the C 2p orbital of rGO to the Sb 4d orbital of $CoSb_2O_6$. For the quantitative analysis of charge transfer, the Bader charge analysis has been performed.[70] As indicated by the Bader charge analysis, $CoSb_2O_6$ gains a charge of 0.74*e*, complemented by a loss of 0.74*e* charge from rGO, having 68 atoms. $CoSb_2O_6$, being more electronegative than rGO, pulls the electron cloud of the C 2p orbitals of rGO towards itself, leading to charge transfer from rGO to $CoSb_2O_6$, which agrees with a recent study on Fe-doped $NiCo_2O_4$@rGO.[71] The charge transfer from rGO to $CoSb_2O_6$ produces a charge redistribution among the atoms in $CoSb_2O_6$.

**3.3.3 Diffusion energy barrier of $Na^+$ ions.** To analyze the mobility of $Na^+$ ions within the system, we have calculated the diffusion energy barrier for both $CoSb_2O_6$ and $CoSb_2O_6$/rGO systems along the path shown in Fig. S22 using DOS calculations. Fig. 9(a) suggests that there is a significant lowering of the diffusion energy barrier upon rGO introduction into $CoSb_2O_6$, as the value is 0.61 eV and 0.15 eV for $CoSb_2O_6$ and $CoSb_2O_6$/rGO, respectively. Pathak *et al.* calculated the diffusion energy barriers of $K^+$, $Na^+$, and $Li^+$ ions on $NiCo_2O_4$ to be 0.48, 0.34, and 0.15 eV, respectively.[72] Therefore, $Na^+$ ions are more mobile in the $CoSb_2O_6$/rGO composite and thus have better charge transfer capability than the pristine one. These findings further justify our experimental observations of enhanced supercapacitance for the $CoSb_2O_6$/rGO composite system. The values for the diffusion energy barrier might vary according to the chosen path.

**3.3.4 Calculation of quantum capacitance.** The quantum capacitance for $CoSb_2O_6$, $CoSb_2O_6$/rGO, and rGO systems has been computed using the quantum capacitance formula:[73]

$$C_Q = e^2 \int_{\infty}^{\infty} D(E) F_T(E - e\varphi_G) dE$$

where $D(E)$ and $\phi_G$ imply the density of states and electrode potential of the system under study, respectively, while the function $F_T(E)$ represents the thermal broadening owing to the thermal effect.

The function $F_T(E)$ can be expressed as

$$F_T(E) = (4k_BT)^{-1}\mathrm{sech}^2(E/2k_BT)$$

The total capacitance of any system can be related to its computed quantum capacitance by the relation:[74]

$$\frac{1}{C_T} = \frac{1}{C_Q} + \frac{1}{C_{EDL}}$$

where $C_{EDL}$ stands for electric double-layer capacitance, which depends on the interfacial interaction between the electrode and electrolyte.

Fig. 9(b) shows the variation of quantum capacitance concerning the electrode potential for $CoSb_2O_6$ and $CoSb_2O_6$/rGO systems. Noticeably, the quantum capacitance is higher for most of the $CoSb_2O_6$/rGO composite electrode potential than for pristine $CoSb_2O_6$. At the Fermi level, the value of quantum capacitance for $CoSb_2O_6$ and $CoSb_2O_6$/rGO is 173.85 and 310.32 mF $cm^{-2}$, respectively. The higher quantum capacitance of the $CoSb_2O_6$/rGO composite leads to a higher total capacitance, thereby achieving better charge storage performance than pristine $CoSb_2O_6$, further supporting our experimental results. Fig. S23 presents the variation of quantum capacitance for rGO. Here, we can observe that the quantum capacitance plot of rGO is graphene-like except for the band gap opening due to the introduction of a functional group, which results in a dip at the Fermi level.[75]

## 4. Conclusion

In summary, we report $CoSb_2O_6$ and $CoSb_2O_6$/rGO composites with different weight ratios of rGO (5%, 10%, 15%, and 20%) synthesized by a hydrothermal reaction and ultrasonic treatment, which show uniform morphology. The $CoSb_2O_6$/rGO_15 composite enables a high specific capacitance of ~1000 F $g^{-1}$ at a mass-normalised current of 2 A $g^{-1}$. The combination of

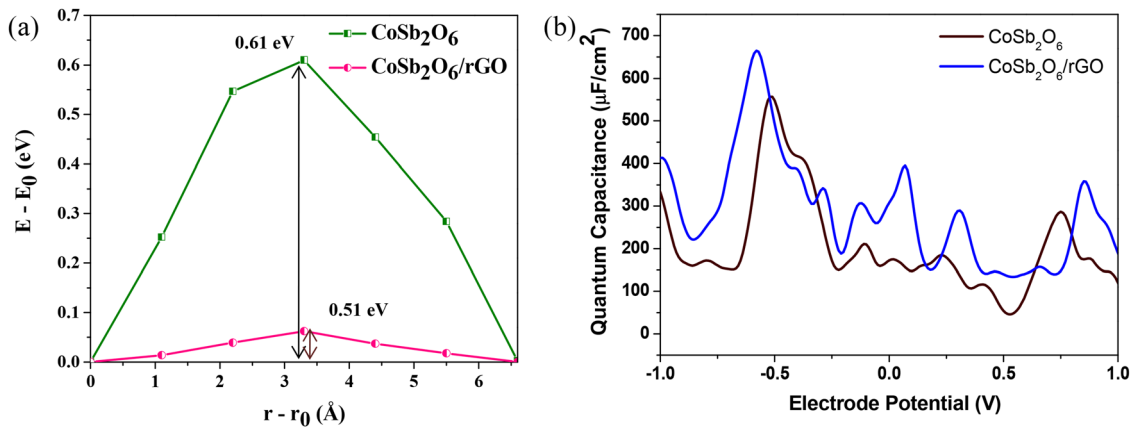


Fig. 9 (a) Diffusion energy plot for the (110) surface of $CoSb_2O_6$ and $CoSb_2O_6$/rGO composite systems and (b) plot of the variation of quantum capacitance with electrode potential for the (110) surface of $CoSb_2O_6$ and $CoSb_2O_6$/rGO composite systems.

$CoSb_2O_6$ and rGO improves the conductivity and stability of pristine $CoSb_2O_6$, resulting in enhanced electrochemical performance of the material. Moreover, when the composite material was assembled into a symmetric supercapacitor device, it exhibited energy and power densities of 38.28 Wh $kg^{-1}$ and 10.08 kW $kg^{-1}$, respectively, and excellent cyclic stability of 98.54% even after 10 000 cycles. The structure and electronic properties, diffusion energy barrier, and the quantum capacitance calculated using density functional theory simulations corroborate our experimental results. The interaction of $CoSb_2O_6$ and rGO due to the charge transfer from rGO to $CoSb_2O_6$ resulted in an enhancement of electronic states near the Fermi level for the $CoSb_2O_6$/rGO composite system. The elevated quantum capacitance and lowered diffusion energy barrier contribute to the enriched charge storage and supercapacitance performance of the $CoSb_2O_6$/rGO composite system, supporting our experimental findings.

## Author contributions

Parul: experimental analysis and writing of the original manuscript draft. Surjit Sahoo: technical discussion and editing. Amrutha M: DFT calculations and theoretical draft write-up. Satyajit Ratha: conceptualization and manuscript editing. Brahmananda Chakraborty: theoretical data supervision and DFT analysis. Saroj Kumar Nayak: manuscript supervision, technical discussion, and funding acquisition. All authors have approved the submission of the final version of the manuscript.

## Conflicts of interest

There are no conflicts to declare.

## Data availability

The data supporting this article have been included as part of the supplementary information (SI). Supplementary information is available. See DOI: https://doi.org/10.1039/d5ma00956a.

## Acknowledgements

The authors acknowledge the financial assistance from NALCO (RP-274), DST, India, and the Ministry of Mines (RP-333) extended to carry out part of this research. Surjit Sahoo gratefully acknowledges the financial support from the Department of Science and Technology (DST), India, under the DST-INSPIRE Faculty Award [DST/INSPIRE/04/2023/000200]. The authors thank Dr Sk Musharaf Ali and Dr Saju Joseph for their constant support and encouragement. They also thank the BARC supercomputing facility and its staff for their valuable assistance and support.

## References

1 S. Sahoo, S. Ratha, C. S. Rout and S. K. Nayak, Self-charging supercapacitors for smart electronic devices: a concise review on the recent trends and future sustainability, *J. Mater. Sci.*, 2022, **57**(7), 4399–4440, DOI: 10.1007/s10853-022-06875-9.

2 S. Sarkis and X. Huang, Cobalt Nanorods as Transition Metal Electrode Materials for Asymmetric Supercapacitor Applications, *J. Phys. Chem. C*, 2020, **124**(38), 20746–20756, DOI: 10.1021/acs.jpcc.0c05562.

3 N. R. Chodankar, *et al.*, True Meaning of Pseudocapacitors and Their Performance Metrics: Asymmetric versus Hybrid Supercapacitors, *Small*, 2020, **16**(37), 2002806, DOI: 10.1002/smll.202002806.

4 A. Jain, *et al.*, Vanadium oxide nanorods as an electrode material for solid state supercapacitor, *Sci. Rep.*, 2022, **12**(1), 21024, DOI: 10.1038/s41598-022-25707-z.

5 S. D. Dhas, *et al.*, Synthesis of NiO nanoparticles for supercapacitor application as an efficient electrode material, *Vacuum*, 2020, **181**, 109646, DOI: 10.1016/j.vacuum.2020.109646.

6 J. Rajeswari, P. S. Kishore, B. Viswanathan and T. K. Varadarajan, One-dimensional $MoO_2$ nanorods for supercapacitor applications, *Electrochem. Commun.*, 2009, **11**(3), 572–575, DOI: 10.1016/j.elecom.2008.12.050.

7 J. Liu, *et al.*, $MnO_2$-based materials for supercapacitor electrodes: challenges, strategies and prospects, *RSC Adv.*, 2022, **12**(55), 35556–35578, DOI: 10.1039/D2RA06664E.

8 C. Yu, M. Moslehpour, T. K. Tran, L. M. Trung, J. P. Ou and N. H. Tien, Impact of non-renewable energy and natural resources on economic recovery: Empirical evidence from selected developing economies, *Resources Policy*, 2023, **80**, 103221, DOI: 10.1016/j.resourpol.2022.103221.

9 M. Pathak, S. M. Jeong and C. S. Rout, Spinel $NiCo_2O_4$ based hybrid materials for supercapacitors: Recent developments and future perspectives, *J. Energy Storage*, 2023, **73**, 108881, DOI: 10.1016/j.est.2023.108881.

10 A. Ansari, R. A. Badhe, D. G. Babar and S. S. Garje, One pot solvothermal synthesis of bimetallic copper iron sulfide ($CuFeS_2$) and its use as electrode material in supercapacitor applications, *Appl. Surf. Sci. Adv.*, 2022, **9**, 100231, DOI: 10.1016/j.apsadv.2022.100231.

11 Y. Guo, Y. Chen, X. Hu, Y. Yao and Z. Li, Tween modified $CuFe_2O_4$ nanoparticles with enhanced supercapacitor performance, *Colloids Surf., A*, 2021, **631**, 127676, DOI: 10.1016/j.colsurfa.2021.127676.

12 J. Sun, C. Xu and H. Chen, A review on the synthesis of $CuCo_2O_4$-based electrode materials and their applications in supercapacitors, *J. Materiomics*, 2021, **7**(1), 98–126, DOI: 10.1016/j.jmat.2020.07.013.

13 V. Gajraj and C. R. Mariappan, $CuWO_4$: a promising multifunctional electrode material for energy storage as in redox active solid-state asymmetric supercapacitor and an electrocatalyst for energy conversion in methanol electro-oxidation, *J. Electroanal. Chem.*, 2021, **895**, 115504, DOI: 10.1016/j.jelechem.2021.115504.

14 N. U. H. Liyakath Ali, *et al.*, Thermo-Electric Powered High Energy-Density Hybrid Supercapattery for Driving Overall Water Splitting: A Novel Trifunctional Builder for Self-Powered Hydrogen Production, *Small*, 2025, **21**(25), 2504667, DOI: 10.1002/smll.202504667.

15 P. R. Bueno, Nanoscale origins of super-capacitance phenomena, *J. Power Sources*, 2019, **414**, 420–434, DOI: 10.1016/j.jpowsour.2019.01.010.
16 N. U. H. L. Ali, P. Pazhamalai, A. Sathyaseelan, R. Swaminathan and S.-J. Kim, Sodium polyacrylate hydrogel electrolyte: Flexible rechargeable supercapacitor using thermally reduced graphene oxide nanosheets, *J. Power Sources*, 2025, **625**, 235648, DOI: 10.1016/j.jpowsour.2024.235648.
17 M. S. Chang, T. Kim, J. H. Kang, J. Park and C. R. Park, The effect of surface characteristics of reduced graphene oxide on the performance of a pseudocapacitor, *2D Mater.*, 2015, **2**(1), 014007, DOI: 10.1088/2053-1583/2/1/014007.
18 S. G. Kandalkar, J. L. Gunjakar and C. D. Lokhande, Preparation of cobalt oxide thin films and its use in supercapacitor application, *Appl. Surf. Sci.*, 2008, **254**(17), 5540–5544, DOI: 10.1016/j.apsusc.2008.02.163.
19 G.-S. Jang, S. Ameen, M. S. Akhtar and H.-S. Shin, Cobalt oxide nanocubes as electrode material for the performance evaluation of electrochemical supercapacitor, *Ceram. Int.*, 2018, **44**(1), 588–595, DOI: 10.1016/j.ceramint.2017.09.217.
20 S. G. Kandalkar, H.-M. Lee, H. Chae and C.-K. Kim, Structural, morphological, and electrical characteristics of the electrodeposited cobalt oxide electrode for supercapacitor applications, *Mater. Res. Bull.*, 2011, **46**(1), 48–51, DOI: 10.1016/j.materresbull.2010.09.041.
21 F. Ali, *et al.*, Capacitive properties of novel Sb-doped $Co_3O_4$ electrode material synthesized by hydrothermal method, *Ceram. Int.*, 2021, **47**(22), 32210–32217, DOI: 10.1016/j.ceramint.2021.08.114.
22 N. Pradeep, V. Chaitra, V. Uma and A. N. Grace, Antimony oxide nanobelts: synthesis by chemical vapour deposition and its characterisation, *Int. J. Nanotechnol.*, 2017, **14**(9–11), 752–761, DOI: 10.1504/IJNT.2017.086761.
23 A. Guillén-Bonilla, *et al.*, Dynamic Response of $CoSb_2O_6$ Trirutile-Type Oxides in a $CO_2$ Atmosphere at Low-Temperatures, *Sensors*, 2014, **14**(9), 15802–15814, DOI: 10.3390/s140915802.
24 X. Zhou, A. Wang, X. Zheng, D. Sun and Y. Yang, Uniformly anchoring $Sb_2O_5$ nanoparticles on graphene sheets via $Co^{2+}$-induced deposition for enhanced lithium/sodium-ion storage, *Inorg. Chem. Front.*, 2024, **11**(14), 4167–4178, DOI: 10.1039/D4QI00827H.
25 U. Ray, D. Das, A. Mitra, K. Das, S. B. Majumder and S. Das, *Cobalt Antimony Oxide-Carbon Black Composite as Negative Electrode for Alkali-Ion Batteries: Synthesis and Electrochemical Characterization*, Social Science Research Network, Rochester, NY, 2023, p. 4608624, DOI: 10.2139/ssrn.4608624.
26 H. Guillén-Bonilla, *et al.*, Sensitivity of Mesoporous $CoSb_2O_6$ Nanoparticles to Gaseous CO and $C_3H_8$ at Low Temperatures, *J. Nanomater.*, 2015, e308465, DOI: 10.1155/2015/308465.
27 J. Sun, B. Luo and H. Li, A Review on the Conventional Capacitors, Supercapacitors, and Emerging Hybrid Ion Capacitors: Past, Present, and Future, *Adv. Energy Sustainability Res.*, 2022, **3**(6), 2100191, DOI: 10.1002/aesr.202100191.
28 O. Ibukun and H. Jeong, Effects of Aqueous Electrolytes in Supercapacitors, *New Phys.: Sae Mulli*, 2019, **69**, 154–158, DOI: 10.3938/NPSM.69.154.
29 A. Guillén-Bonilla, *et al.*, Synthesis and characterization of cobalt antimonate nanostructures and their study as potential CO and $CO_2$ sensor at low temperatures, *J. Mater. Sci.: Mater. Electron.*, 2018, **29**(18), 15632–15642, DOI: 10.1007/s10854-018-9157-2.
30 K. M. Anilkumar, M. Manoj, B. Jinsiha, V. S. Pradeep and S. Jayalekshmi, $Mn_3O_4$/reduced graphene oxide nanocomposite electrodes with tailored morphology for high power supercapacitor applications, *Electrochim. Acta*, 2017, **236**, 424–433, DOI: 10.1016/j.electacta.2017.03.167.
31 M. A. Garakani, *et al.*, Scalable spray-coated graphene-based electrodes for high-power electrochemical double-layer capacitors operating over a wide range of temperature, *Energy Storage Mater.*, 2021, **34**, 1–11, DOI: 10.1016/j.ensm.2020.08.036.
32 C. Lämmel, M. Schneider, M. Weiser and A. Michaelis, Investigations of electrochemical double layer capacitor (EDLC) materials – a comparison of test methods, *Materialwiss. Werkstofftech.*, 2013, **44**(7), 641–649, DOI: 10.1002/mawe.201300122.
33 P. E. Blöchl, Projector augmented-wave method, *Phys. Rev. B: Condens. Matter Mater. Phys.*, 1994, **50**(24), 17953–17979, DOI: 10.1103/PhysRevB.50.17953.
34 G. Kresse and D. Joubert, From ultrasoft pseudopotentials to the projector augmented-wave method, *Phys. Rev. B: Condens. Matter Mater. Phys.*, 1999, **59**(3), 1758–1775, DOI: 10.1103/PhysRevB.59.1758.
35 Z. Wu and R. E. Cohen, More accurate generalized gradient approximation for solids, *Phys. Rev. B: Condens. Matter Mater. Phys.*, 2006, **73**(23), 235116, DOI: 10.1103/PhysRevB.73.235116.
36 S. Grimme, Semiempirical GGA-type density functional constructed with a long-range dispersion correction, *J. Comput. Chem.*, 2006, **27**(15), 1787–1799, DOI: 10.1002/jcc.20495.
37 M. J. Kruszewski, K. Cymerman, E. Choińska, D. Moszczyńska and Ł. Ciupiński, A comparative study of oxidation behavior of $Co_4Sb_{12}$ and $Co_4Sb_{10.8}Se_{0.6}Te_{0.6}$ skutterudite thermoelectric materials fabricated via fast SHS-PPS route, *J. Eur. Ceram. Soc.*, 2024, **44**(6), 3760–3766, DOI: 10.1016/j.jeurceramsoc.2024.01.044.
38 H. Jensen, *et al.*, Determination of size distributions in nanosized powders by TEM, XRD, and SAXS, *J. Exp. Nanosci.*, 2006, **1**(3), 355–375, DOI: 10.1080/17458080600752482.
39 S. Kumuda, U. Gandhi, U. Mangalanathan and K. Rajanna, Synthesis and characterization of graphene oxide and reduced graphene oxide chemically reduced at different time duration, *J. Mater. Sci.: Mater. Electron.*, 2024, **35**(9), 637, DOI: 10.1007/s10854-024-12393-y.
40 L. G. Cançado, *et al.*, General equation for the determination of the crystallite size La of nanographite by Raman spectroscopy, *Appl. Phys. Lett.*, 2006, **88**(16), 163106, DOI: 10.1063/1.2196057.
41 T. J. Chuang, C. R. Brundle and D. W. Rice, Interpretation of the X-ray photoemission spectra of cobalt oxides and cobalt oxide surfaces, *Surf. Sci.*, 1976, **59**(2), 413–429, DOI: 10.1016/0039-6028(76)90026-1.
42 T. A. Evans and K.-S. Choi, Electrochemical Synthesis and Investigation of Stoichiometric, Phase-Pure $CoSb_2O_6$ and $MnSb_2O_6$ Electrodes for the Oxygen Evolution Reaction in

Acidic Media, *ACS Appl. Energy Mater.*, 2020, **3**(6), 5563–5571, DOI: 10.1021/acsaem.0c00526.

43 Z. Li, X. Song, S. Cui, Y. Jiao and C. Zhou, Fabrication of macroporous reduced graphene oxide composite aerogels reinforced with chitosan for high bilirubin adsorption, *RSC Adv.*, 2018, **8**(15), 8338–8348, DOI: 10.1039/C8RA00358K.

44 Z. Chen, *et al.*, Nanoarchitectured $Co_3O_4$/reduced graphene oxide as anode material for lithium-ion batteries with enhanced cycling stability, *Ionics*, 2019, **25**(12), 5779–5786, DOI: 10.1007/s11581-019-03134-x.

45 P. Lin, *et al.*, The Nickel Oxide/CNT Composites with High Capacitance for Supercapacitor, *J. Electrochem. Soc.*, 2010, **157**(7), A818, DOI: 10.1149/1.3425624.

46 Parul, S. Sahoo, S. Ratha, G. Sanyal, B. Chakraborty and S. K. Nayak, Experimental and theoretical investigation on the charge storage performance of $NiSb_2O_6$ and its reduced graphene oxide composite – a comparative analysis, *Phys. Chem. Chem. Phys.*, 2024, **26**(48), 29962–29975, DOI: 10.1039/D4CP03249G.

47 G. He, *et al.*, Hydrothermal preparation of $Co_3O_4$@graphene nanocomposite for supercapacitor with enhanced capacitive performance, *Mater. Lett.*, 2012, **82**, 61–63, DOI: 10.1016/j.matlet.2012.05.048.

48 J. Jayachandiran, *et al.*, Synthesis and Electrochemical Studies of rGO/ZnO Nanocomposite for Supercapacitor Application, *J. Inorg. Organomet. Polym.*, 2018, **28**(5), 2046–2055, DOI: 10.1007/s10904-018-0873-0.

49 M. Chandel, D. Moitra, P. Makkar, H. Sinha, H. S. Hora and N. N. Ghosh, Synthesis of multifunctional $CuFe_2O_4$-reduced graphene oxide nanocomposite: an efficient magnetically separable catalyst as well as high performance supercapacitor and first-principles calculations of its electronic structures, *RSC Adv.*, 2018, **8**(49), 27725–27739, DOI: 10.1039/C8RA05393F.

50 D. Govindarajan, V. Uma Shankar and R. Gopalakrishnan, Supercapacitor behavior and characterization of RGO anchored $V_2O_5$ nanorods, *J. Mater. Sci.: Mater. Electron.*, 2019, **30**(17), 16142–16155, DOI: 10.1007/s10854-019-01984-9.

51 N. A. Devi, *et al.*, Investigation of chemical bonding and supercapacitivity properties of Fe3O4-rGO nanocomposites for supercapacitor applications, *Diamond Relat. Mater.*, 2020, **104**, 107756, DOI: 10.1016/j.diamond.2020.107756.

52 I. Kotutha, T. Duangchuen, E. Swatsitang, W. Meewasana, J. Khajonrit and S. Maensiri, Electrochemical properties of rGO/$CoFe_2O_4$ nanocomposites for energy storage application, *Ionics*, 2019, **25**(11), 5401–5409, DOI: 10.1007/s11581-019-03114-1.

53 S. Ghosh, P. Samanta, P. Samanta, N. C. Murmu and T. Kuila, Investigation of Electrochemical Charge Storage Efficiency of $NiCo_2Se_4$/RGO Composites Derived at Varied Duration and Its Asymmetric Supercapacitor Device, *Energy Fuels*, 2020, **34**(10), 13056–13066, DOI: 10.1021/acs.energyfuels.0c02152.

54 B. Rani and N. K. Sahu, Electrochemical properties of $CoFe_2O_4$ nanoparticles and its rGO composite for supercapacitor, *Diamond Relat. Mater.*, 2020, **108**, 107978, DOI: 10.1016/j.diamond.2020.107978.

55 C. Xiang, M. Li, M. Zhi, A. Manivannan and N. Wu, A reduced graphene oxide/$Co_3O_4$ composite for supercapacitor electrode, *J. Power Sources*, 2013, **226**, 65–70, DOI: 10.1016/j.jpowsour.2012.10.064.

56 A. C. Lazanas and M. I. Prodromidis, Electrochemical Impedance Spectroscopy–A Tutorial, *ACS Meas. Sci. Au*, 2023, **3**(3), 162–193, DOI: 10.1021/acsmeasuresciau.2c00070.

57 S. A. El-Khodary, *et al.*, Sonochemical assisted fabrication of 3D hierarchical porous carbon for high-performance symmetric supercapacitor, *Ultrason. Sonochem.*, 2019, **58**, 104617, DOI: 10.1016/j.ultsonch.2019.104617.

58 Z.-H. Huang, T.-Y. Liu, Y. Song, Y. Li and X.-X. Liu, Balancing the electrical double layer capacitance and pseudocapacitance of hetero-atom doped carbon, *Nanoscale*, 2017, **9**(35), 13119–13127, DOI: 10.1039/C7NR04234E.

59 J. Liu, *et al.*, Advanced Energy Storage Devices: Basic Principles, Analytical Methods, and Rational Materials Design, *Adv. Sci.*, 2018, **5**(1), 1700322, DOI: 10.1002/advs.201700322.

60 Y. Lan, *et al.*, Phosphorization Boosts the Capacitance of Mixed Metal Nanosheet Array for High Performance Supercapacitor Electrode, *Nanoscale*, 2018, **10**(25), 11775–11781, DOI: 10.1039/C8NR01229F.

61 Y. Wang, *et al.*, Intercalating Ultrathin MoO3 Nanobelts into MXene Film with Ultrahigh Volumetric Capacitance and Excellent Deformation for High-Energy-Density Devices, *Nano-Micro Lett.*, 2020, **12**(1), 115, DOI: 10.1007/s40820-020-00450-0.

62 S. Dutt, *et al.*, Flexible and Highly Stable Textile-Based Symmetric Supercapacitor Comprising Binder-Free $MnO_2$/rGO-CF Nanocomposite Electrodes, *J. Electron. Mater.*, 2023, **52**(11), 7447–7458, DOI: 10.1007/s11664-023-10683-5.

63 M. Kour, *et al.*, Highly stable electrodeposited 2D $Mn_{0.2}Co_{0.8}$ LDH nanoplatelets based symmetric supercapacitor electrode, *Mater. Sci. Eng., B*, 2023, **293**, 116488, DOI: 10.1016/j.mseb.2023.116488.

64 I. Rabani, *et al.*, 1D-CoSe 2 nanoarray: a designed structure for efficient hydrogen evolution and symmetric supercapacitor characteristics, *Dalton Trans.*, 2020, **49**(40), 14191–14200, DOI: 10.1039/D0DT02548H.

65 U. M. Patil, *et al.*, Enhanced Symmetric Supercapacitive Performance of $Co(OH)_2$ Nanorods Decorated Conducting Porous Graphene Foam Electrodes, *Electrochim. Acta*, 2014, **129**, 334–342, DOI: 10.1016/j.electacta.2014.02.063.

66 M. Murugan, *et al.*, Development of Mesoporous Carbon Composites with Waste Plastics Derived Graphene and $MnO_2$ for Supercapacitor Applications, *J. Electrochem. Soc.*, 2023, **170**(4), 040518, DOI: 10.1149/1945-7111/acbf7b.

67 V. Sahu, S. Goel, R. Kishore Sharma and G. Singh, Zinc oxide nanoring embedded lacey graphene nanoribbons in symmetric/asymmetric electrochemical capacitive energy storage, *Nanoscale*, 2015, **7**(48), 20642–20651, DOI: 10.1039/C5NR06083D.

68 N. Kumar, T. A. Wani, P. K. Pathak, A. Bera and R. R. Salunkhe, Multifunctional nanoarchitectured porous carbon for solar steam generation and supercapacitor applications, *Sustainable Energy Fuels*, 2022, **6**(7), 1762–1769, DOI: 10.1039/D2SE00092J.

69 A. Guillén-Bonilla, *et al.*, Dynamic Response of $CoSb_2O_6$ Trirutile-Type Oxides in a $CO_2$ Atmosphere at Low-Temperatures, *Sensors*, 2014, **14**(9), 15802–15814, DOI: 10.3390/s140915802.
70 E. Sanville, S. D. Kenny, R. Smith and G. Henkelman, Improved grid-based algorithm for Bader charge allocation, *J. Comput. Chem.*, 2007, **28**(5), 899–908, DOI: 10.1002/jcc.20575.
71 S. Abbas, *et al.*, Fe doped $NiCo_2O_4$@rGO nanosheets network boost electrochemical kinetics for high energy density and stable asymmetric coin cell supercapacitor, *J. Energy Storage*, 2024, **102**, 114181, DOI: 10.1016/j.est.2024.114181.
72 M. Pathak, J. R. Jose, B. Chakraborty and C. S. Rout, High performance supercapacitor electrodes based on spinel $NiCo_2O_4$@MWCNT composite with insights from density functional theory simulations, *J. Chem. Phys.*, 2020, **152**(6), 064706, DOI: 10.1063/1.5138727.
73 G. M. Yang, H. Z. Zhang, X. F. Fan and W. T. Zheng, Density Functional Theory Calculations for the Quantum Capacitance Performance of Graphene-Based Electrode Material, *J. Phys. Chem. C*, 2015, **119**(12), 6464–6470, DOI: 10.1021/jp512176r.
74 C. Zhan, J. Neal, J. Wu and D. Jiang, Quantum Effects on the Capacitance of Graphene-Based Electrodes, *J. Phys. Chem. C*, 2015, **119**(39), 22297–22303, DOI: 10.1021/acs.jpcc.5b05930.
75 C. Zhan, J. Neal, J. Wu and D. Jiang, Quantum Effects on the Capacitance of Graphene-Based Electrodes, *J. Phys. Chem. C*, 2015, **119**(39), 22297–22303, DOI: 10.1021/acs.jpcc.5b05930.